

# Ripples and dunes in a turbulent stream. Part 1: Turbulent flow over a wavy bottom

By ANTOINE FOURRIÈRE, PHILIPPE CLAUDIN  
AND BRUNO ANDREOTTI

Laboratoire de Physique et Mécanique des Milieux Hétérogènes  
PMMH UMR 7636 CNRS-ESPCI-P6-P7,  
10 rue Vauquelin, 75231 Paris Cedex 05, France.

(Received 24 September 2007)

Using a second order turbulent closure, the turbulent flow over a wavy bottom is derived as a systematic expansion with respect to the amplitude of the corrugation. The article is focused on the analysis of the dynamical mechanisms controlling the different regions of the flow. It aims also at calculating the shear and normal stresses applied to the ground, which constitute key ingredients of the morphodynamics of ripples and dunes. Amongst the non-linear effects, we investigate the relation between the geometry of the bottom and the resulting hydrodynamical roughness. We also show that most of the first non-linearities exert a negative feedback on the basal stress. Finally, we study the influence of the presence of a free surface at distance from the ground comparable to the bottom wavelength. Due to the resonance of gravity surface waves, the phase lag between the shear stress and the bottom profile shifts downstream. This is a crucial point to understand ripples and dunes instabilities, detailed in part 3.

---

## 1. Introduction

The formation of ripples and dunes at the surface of an erodible sand bed results from the interplay between the relief, the flow and the sediment transport. The aim of this article is to propose a coherent and detailed picture of the phenomenon in the important case of a unidirectional turbulent stream. The first part is devoted to the study of the stationary flow over a wavy rough bottom. In the second part we propose a common theoretical description of the different modes of sediment transport. In the third and last part, we revisit the linear instability of a flat sand bed submitted to a water shear flow and show that, by contrast to that of ripples, the formation of sub-aqueous dunes is non-linear and therefore cannot be described by a linear model.

It has long been recognised that the mechanism responsible for the formation and growth of bedforms is related to the phase-lag between sediment transport and bed elevation (Kennedy 1963, Reynolds 1965). It has been shown in the context of aeolian dunes that this lag comes from two contributions, which can be considered as independent as the time scale involved in the bed evolution is much slower than the hydrodynamics relaxation (Kroy & al. 2002). First there is a shift between the bed and the basal shear stress profiles, a shift which results from the hydrodynamics only. Its sign is not obvious *a priori* and the stress maximum can be either upstream or downstream the bed crest depending on the topography. The second contribution comes from the transport: the sediment flux needs some time to adapt to some imposed shearing. This relaxation mechanism induces a downstream lag of the flux with respect to the shear.

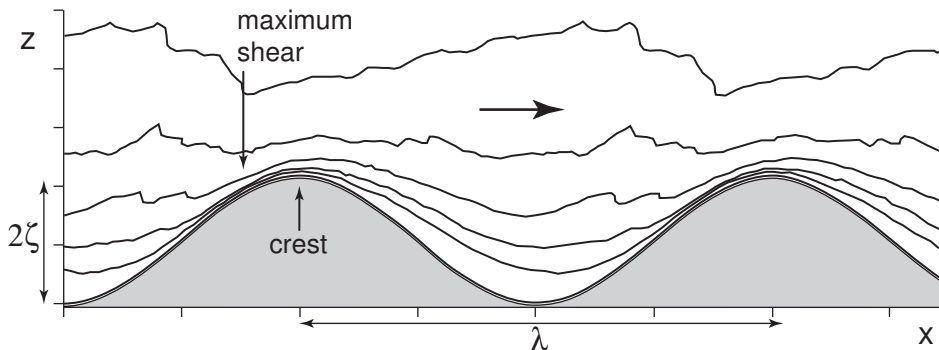


FIGURE 1. Iso-velocity lines over a wavy bottom (data after Poggi et al. 2007). The fluid is flowing from left to right along the  $x$ -axis.  $z$  is perpendicular. The bottom profile is  $z = Z(x) = \zeta \cos(kx)$ . In that experiment, the wavelength and amplitude of the bumps are  $\lambda = 2\pi/k = 3.2$  m and  $\zeta = 0.08$  m, for a water depth  $H = 0.6$  m). The point of maximum shear on the bump is located upstream the crest.

When the sum of these two contributions results in a maximum flux upstream the bed crest, sediment deposition occurs on the bump, leading to an unstable situation and thus to the amplification of the bedform. Conversely, when the phase-lag between transport and bed profiles moves the maximum flux downstream the crest, the bump is eroded and the bedform cannot grow. In this part 1, we shall focus on the first of these contributions, the second one being treated in the part 2.

In order to obtain the basal shear stress and in particular its phase, we consider the generic case of a turbulent flow over a fixed sinusoidal bottom of wavelength  $\lambda$  (see figure 1 for an illustration of the geometry and for the main notations). In the viscous limit, the hydrodynamics has been solved rigorously and analytically by Charru & Hinch 2000. The turbulent case is more problematic as it requires the introduction of a turbulent closure. The first attempts to model turbulence in this geometry have dealt with potential flows (Kennedy 1963, Reynolds 1965, Parker 1975, Coleman & Fenton 2000), for which the velocity field does not present any lag with respect to the boundary. The shallow-water approximation (Gradowczyk 1970) implies that the ripples spread their influence on the whole depth of the flow. However, patterns at small wavelength  $\lambda$  only have an influence within a vertical distance of the order of  $\lambda$  from the boundary. It is then crucial to compute the shape of the modes explicitly, taking into account the rotational character of the flow (Engelund 1970, Smith 1970, Fredsøe 1974).

We revisit the problem, following an approach initiated in four important articles. The first is due to Jackson & Hunt 1975 who have analytically computed the shear stress for asymptotically large patterns, in the absence of free surface. Richards 1980 used a  $k$ -epsilon closure and investigated the presence of a free surface. In the context of computational fluid dynamics, ? have compared the influence of the closure scheme on the linear flow over a relief. More recently, Colombini 2004, Colombini & Stocchino 2004 have computed numerically the flow over ripples and dunes using a Prandtl mixing length closure. Experimental data as well as large eddy simulations of this type of flow are also available (see e.g. Gong et al. 1996, Henn & Sykes 1999, Poggi et al. 2007).

Here, our goal is not to provide a new closure or a new computational technique – except for the noticeable non-linear calculations, our modeling is very close in spirit to that of Colombini 2004 – but rather to address new questions, or to revisit issues, related to the development of ripples and dunes. What is the range of amplitudes in which the linear approximation is quantitatively valid? How can we describe the separation of

streamlines and the formation of a recirculation bubble in the lee sides of the bumps? Is there a direct proportionality between the geometrical bottom roughness and the hydrodynamical one? What is the physical origin of the phase lag between the bottom shear stress and the relief? What is the effect of the corrugation amplitude on this phase? What is the effect of the free surface? Is it responsible for a new instability, namely that of dunes?

The article is structured as follows. In the next section, we derive a non-linear solution for the structure of the turbulent flow just above the wavy bottom. In section 3, we study the linear solution in the case of wavelengths much smaller than the flow depth. Section 4 is devoted to the derivation of the first non-linear corrections. We discuss in particular the effect of the bottom corrugation on the apparent roughness far from the boundary. Finally, we investigate the effect of the free surface in the case of wavelengths comparable or larger than the flow depth (section 5) and derive a simple – analytically tractable – friction force model whose results compare well with those of the full equations (section 6).

## 2. Surface layer

### 2.1. Turbulent flow over a uniform bottom

We consider the turbulent flow over a relief. Following the Reynolds decomposition between average quantities and fluctuating ones (denoted with a prime), the equations governing the mean velocity field  $u_i$  can be written as:

$$\partial_i u_i = 0, \quad (2.1)$$

$$D_t u_i = \partial_t u_i + u_j \partial_j u_i = -\partial_j \tau_{ij} - \partial_i p, \quad (2.2)$$

where  $\tau_{ij} = \overline{u'_i u'_j}$  is the Reynolds stress tensor (?). For the sake of simplicity, we omit the density factor  $\rho$  in front of the pressure  $p$  and the stress tensor. The aim of this paper is to describe quantitatively the stationary flow (in a statistical sense) over a fixed corrugated boundary within this framework.

The reference state is the homogeneous and steady flow over a flat bottom, submitted to an imposed constant shear stress  $\tau_{xz} = -u_*^2$ . This bottom is assumed to be characterised by an hydrodynamical roughness  $z_0$ . In the absence of transport,  $z_0$  is usually related to the geometrical bottom roughness, i.e. to the grain diameter  $d$  or to the wavelength and amplitude of the ripples, depending on the scale considered. It is precisely one of the goals of the present paper to establish the connection between geometrical and hydrodynamical roughness'. In the case of dunes, when the flow velocity is sufficiently large to transport sediments, the negative feedback of the moving particles on the flow modifies the velocity profile close to the bottom. We will detail the feedback mechanisms and discuss the relation between the apparent roughness and the wind speed in the part 2. For now,  $z_0$  is assumed to be a known parameter. In most of the relevant situations,  $z_0$  is larger than the viscous sublayer thickness. In this case, it is well known that the velocity has a single non zero component along the  $x$ -axis, which increases logarithmically with  $z$  (Tritton 1988):

$$u_x = \frac{u_*}{\kappa} \ln \left( 1 + \frac{z}{z_0} \right). \quad (2.3)$$

The velocity is assumed to vanish on the bottom ( $z = 0$ ). We emphasize again that this is still valid in the case of bed load transport, provided a redefinition of  $z = 0$  and  $z_0$  (see part 2).

This logarithmic profile is consistent with a first order turbulent closure between the shear stress and the velocity gradient

$$\tau_{xz} = -\kappa^2 L^2 |\partial_z u_x| \partial_z u_x, \quad (2.4)$$

where the mixing length is  $L = z + z_0$  and  $\kappa \simeq 0.4$  is the von Kármán constant. As originally shown by Prandtl 1925, this results from dimensional analysis: as the turbulent regime is characterised by the absence of any intrinsic length and time scales, the only way to construct a diffusive flux is to take the velocity gradient  $|\partial_z u_x|$  as the relevant mixing frequency and the geometrical distance to the bottom as the relevant mixing length scale. Similarly, the normal stresses can be written as:

$$\tau_{xx} = \tau_{yy} = \tau_{zz} = \frac{1}{3} \tau_{ll}, \quad (2.5)$$

$$\tau_{ll} = \kappa^2 \chi^2 L^2 |\partial_z u_x|^2, \quad (2.6)$$

where  $\chi$  is a second phenomenological constant estimated in the range 2.5 – 3. Note that  $\chi$  does not have any influence on the results as it describes the isotropic component of the Reynolds stress tensor, which can be absorbed into the pressure terms.

Introducing the strain rate tensor  $\dot{\gamma}_{ij} = \partial_i u_j + \partial_j u_i$  and its squared modulus  $|\dot{\gamma}|^2 = \frac{1}{2} \dot{\gamma}_{ij} \dot{\gamma}_{ij}$ , we can write the above expressions in a general tensorial form:

$$\tau_{ij} = \kappa^2 L^2 |\dot{\gamma}| \left( \frac{1}{3} \chi^2 |\dot{\gamma}| \delta_{ij} - \dot{\gamma}_{ij} \right). \quad (2.7)$$

## 2.2. A second order turbulent closure

As already stated in the introduction, to solve quantitatively the ‘dune problem’, we need to take correctly into account the effects inducing a phase shift between the stresses and the relief. As a matter of fact, a first order closure assumes that the turbulent energy adapts instantaneously to the mean strain tensor. To take into account the lag between the stress and the strain tensors, one needs to formulate a second order turbulent closure. The dynamical equations governing the second-order moments  $\tau_{ik}$  can be derived rigorously. Under the assumption of turbulence isotropy at the dissipative scale, it can be written under the form:

$$D_t \tau_{ik} = \partial_t \tau_{ik} + u_j \partial_j \tau_{ik} = -\tau_{kj} \partial_j u_i - \tau_{ij} \partial_j u_k - \partial_j \phi_{ik} - \pi_{ik} - \frac{2}{3} \delta_{ik} \varepsilon. \quad (2.8)$$

$\varepsilon$  is the dissipation rate;  $\phi_{ik} = \overline{u'_i u'_j u'_k}$  is the spatial flux of turbulent energy induced by fluctuations; the pressure term  $\pi_{ik} = \overline{u'_k \partial_i p'} + \overline{u'_i \partial_k p'}$  conserves energy and is usually responsible for the isotropisation of fluctuations.

We wish also to keep a model sufficiently simple to allow for an analysis of the results in term of dynamical mechanisms. Here, we simply assume that the stress tensor relaxes towards its steady state expression prescribed by equation (2.7). Again, for dimensional reasons, we write the relaxation rate under the form  $|\dot{\gamma}|/\beta$ , where  $\beta$  is a phenomenological constant, and keep the mixing length  $L$  fixed by the geometrical distance to the wall. The second moment equation then takes the form of a first order relaxation equation:

$$D_t \tau_{ik} = \partial_t \tau_{ik} + u_j \partial_j \tau_{ik} = \frac{|\dot{\gamma}|}{\beta} \left[ \kappa^2 L^2 \left( \delta_{ij} \frac{1}{3} \chi^2 |\dot{\gamma}|^2 - |\dot{\gamma}| \dot{\gamma}_{ij} \right) - \tau_{ij} \right]. \quad (2.9)$$

Setting  $\beta = 0$ , one recovers the stationary solutions (2.7). A finite value of  $\beta$  introduces a lag between a change of the flow velocity field and the point/time at which the Reynolds stress readapts to this change.

### 2.3. Equations for 2D steady flows

In this paper, we focus on 2D steady situations, i.e. geometries invariant along the  $y$ -direction, see figure 1. As they are of permanent use for the rest of the paper, we express the components of the velocity and stress dynamical equations in the  $x$  and  $z$  directions. The Navier-Stokes equations read:

$$\partial_x u_x + \partial_z u_z = 0, \quad (2.10)$$

$$u_x \partial_x u_x + u_z \partial_z u_x = -\partial_x p - \partial_z \tau_{xz} - \partial_x \tau_{xx}, \quad (2.11)$$

$$u_x \partial_x u_z + u_z \partial_z u_z = -\partial_z p - \partial_z \tau_{zz} - \partial_x \tau_{zx}, \quad (2.12)$$

and the stress relaxation equations are the following:

$$u_x \partial_x \tau_{xz} + u_z \partial_z \tau_{xz} = \frac{|\dot{\gamma}|}{\beta} [-\kappa^2 L^2 |\dot{\gamma}| \dot{\gamma}_{xz} - \tau_{xz}], \quad (2.13)$$

$$u_x \partial_x \tau_{xx} + u_z \partial_z \tau_{xx} = \frac{|\dot{\gamma}|}{\beta} \left[ -\kappa^2 L^2 |\dot{\gamma}| \dot{\gamma}_{xx} + \frac{1}{3} \kappa^2 \chi^2 L^2 |\dot{\gamma}|^2 - \tau_{xx} \right], \quad (2.14)$$

$$u_x \partial_x \tau_{zz} + u_z \partial_z \tau_{zz} = \frac{|\dot{\gamma}|}{\beta} \left[ -\kappa^2 L^2 |\dot{\gamma}| \dot{\gamma}_{zz} + \frac{1}{3} \kappa^2 \chi^2 L^2 |\dot{\gamma}|^2 - \tau_{zz} \right]. \quad (2.15)$$

In these expressions, the strain tensor components are given by

$$\dot{\gamma}_{xz} = \dot{\gamma}_{zx} = \partial_z u_x + \partial_x u_z, \quad \dot{\gamma}_{xx} = 2\partial_x u_x \quad \text{and} \quad \dot{\gamma}_{zz} = 2\partial_z u_z = -\dot{\gamma}_{xx}, \quad (2.16)$$

and the strain modulus by:

$$|\dot{\gamma}|^2 = 2(\partial_x u_x)^2 + 2(\partial_z u_z)^2 + (\partial_z u_x + \partial_x u_z)^2 = 4(\partial_x u_x)^2 + (\partial_z u_x + \partial_x u_z)^2. \quad (2.17)$$

### 2.4. Surface boundary layer

We first wish to solve the problem of the flow over the surface of the bottom under the boundary layer assumption. For this, we consider a layer of typical depth  $\zeta$  above the surface characterised by a typical horizontal scale  $\lambda$  – later on,  $\lambda$  will denote the wavelength of the bottom corrugation and  $2\zeta$  its amplitude. The full dynamical equations can be simplified in the limit  $\zeta/\lambda \ll 1$ . From the equation of continuity, we get the relation between the orders of magnitude of the vertical and horizontal velocities:

$$\mathcal{O}(u_z) = \frac{\zeta}{\lambda} \mathcal{O}(u_x). \quad (2.18)$$

The shear rate thus goes like  $\mathcal{O}(|\dot{\gamma}|) = \mathcal{O}(\dot{\gamma}_{xz}) = \mathcal{O}(u_x)/\zeta$ , and the anisotropy of the normal strain rates as well as that of the normal stresses is negligible:  $\mathcal{O}(\dot{\gamma}_{zz} - \dot{\gamma}_{xx}) = \mathcal{O}(u_x)/\lambda \ll \mathcal{O}(|\dot{\gamma}|)$ . We introduce the notation  $\wp = p + \tau_l/3$  for the pressure. The Navier-Stokes equations then simplify into

$$\partial_z \wp = 0 \quad \text{and} \quad \partial_x \wp + \partial_z \tau_{xz} = 0. \quad (2.19)$$

The surface boundary layer is characterised by a unique dimensionless parameter  $\mathcal{A}$ , which compares the driving by the pressure gradient and that by the basal shear stress  $\tau_b \equiv |u_b|u_b$ :

$$\mathcal{A} \equiv \frac{z_0 \partial_x \wp}{|u_b|u_b}. \quad (2.20)$$

As seen in figure 2, a negative value of  $\mathcal{A}$  corresponds to situations where the two driving forces have opposite directions. As the pressure  $\wp$  does not depend on  $z$ , one can integrate

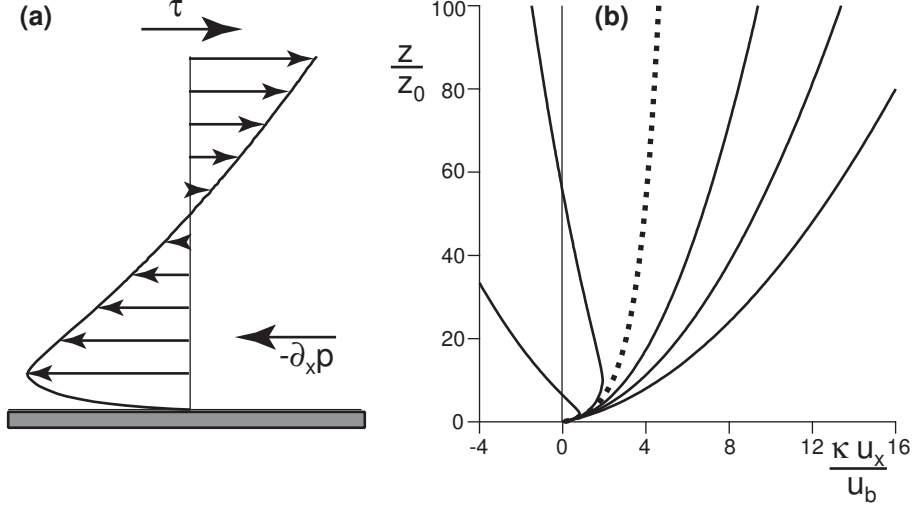


FIGURE 2. (a) Schematic of the generic boundary layer entrained both by a shear stress  $\tau$  and a pressure gradient  $\partial_x p$ . When the two effects are antagonists, a recirculation zone may appear close to the boundary. (b) Velocity vertical profiles for different values of the parameter  $\mathcal{A}$  comparing the shear stress and the pressure gradient effect (from left to right:  $-0.5$ ,  $-0.1$ ,  $0$ ,  $0.2$ ,  $0.5$  and  $1$ ). The curve  $\mathcal{A} = 0$  (dotted line) corresponds to the logarithmic case  $u_x \propto \ln(1 + z/z_0)$ . Note that the sign of the velocity changes for  $\mathcal{A} < 0$ . The height at which the velocity vanishes scales roughly as  $-1/\mathcal{A}$ .

the above equation into:

$$\tau_{xz} = -|u_b|u_b - z\partial_x \wp = -|u_b|u_b|s|s, \quad \text{with} \quad |s|s = 1 + \mathcal{A} \frac{z}{z_0}. \quad (2.21)$$

The convective terms of the shear stress relaxation equation (2.13) are smaller than the right hand side terms by a factor  $\zeta/\lambda$ . As a consequence, the stress-strain relation reduces to  $\tau_{xz} = -\kappa^2(z + z_0)^2|\dot{\gamma}|\dot{\gamma}_{xz}$ , where  $z$  denotes the vertical distance to the floor. We then get the differential equation:

$$\frac{\partial u_x}{\partial s} = \frac{2u_b}{\kappa} \left[ 1 - \frac{\mathcal{A} - 1}{|s|s + \mathcal{A} - 1} \right]. \quad (2.22)$$

whose solution depends on the sign of  $s$ .

*First case:  $s > 0$*  - The assumption of a positive  $s$  corresponds either to  $\mathcal{A} > 0$  or to  $\mathcal{A} < 0$  and  $\mathcal{A}z/z_0 > -1$ . The velocity can be expressed as:

$$\frac{\kappa u_x}{2u_b} = \int_1^s \left[ 1 - \frac{\mathcal{A} - 1}{\sigma^2 + \mathcal{A} - 1} \right] d\sigma. \quad (2.23)$$

For  $\mathcal{A} < 1$  this immediately integrates into:

$$\begin{aligned} \frac{\kappa u_x}{2u_b} &= s - 1 + \frac{1}{2}\sqrt{1 - \mathcal{A}} \ln \left( \frac{s - \sqrt{1 - \mathcal{A}}}{s + \sqrt{1 - \mathcal{A}}} \times \frac{1 + \sqrt{1 - \mathcal{A}}}{1 - \sqrt{1 - \mathcal{A}}} \right) \\ &= \sqrt{1 + \mathcal{A} \frac{z}{z_0}} - 1 + \frac{1}{2}\sqrt{1 - \mathcal{A}} \ln \left( \frac{\sqrt{1 + \mathcal{A}z/z_0} - \sqrt{1 - \mathcal{A}}}{\sqrt{1 + \mathcal{A}z/z_0} + \sqrt{1 - \mathcal{A}}} \times \frac{1 + \sqrt{1 - \mathcal{A}}}{1 - \sqrt{1 - \mathcal{A}}} \right). \end{aligned} \quad (2.24)$$

Now, for  $\mathcal{A} > 1$  we get instead:

$$\begin{aligned} \frac{\kappa u}{2u_b} &= s - 1 - \sqrt{\mathcal{A} - 1} \left[ \arctan \frac{s}{\sqrt{\mathcal{A} - 1}} - \arctan \frac{1}{\sqrt{\mathcal{A} - 1}} \right] \\ &= \sqrt{1 + \mathcal{A}z/z_0} - 1 - \sqrt{\mathcal{A} - 1} \left[ \arctan \sqrt{\frac{1 + \mathcal{A}z/z_0}{\mathcal{A} - 1}} - \arctan \frac{1}{\sqrt{\mathcal{A} - 1}} \right]. \end{aligned} \quad (2.25)$$

*Second case:*  $s < 0$  – The assumption of a negative  $s$  corresponds to  $\mathcal{A} < 0$  and  $z > -z_0/\mathcal{A}$ . We thus have now to integrate

$$\frac{\kappa u}{2u_b} = \int_0^s \left[ 1 - \frac{1 - \mathcal{A}}{\sigma^2 + 1 - \mathcal{A}} \right] d\sigma + \int_1^0 \left[ 1 - \frac{\mathcal{A} - 1}{\sigma^2 + \mathcal{A} - 1} \right] d\sigma, \quad (2.26)$$

which gives

$$\begin{aligned} \frac{\kappa u_x}{2u_b} &= s - 1 + \sqrt{1 - \mathcal{A}} \left[ \frac{1}{2} \ln \left( \frac{\sqrt{1 - \mathcal{A}} + 1}{\sqrt{1 - \mathcal{A}} - 1} \right) - \arctan \frac{s}{\sqrt{1 - \mathcal{A}}} \right] \\ &= -\sqrt{-1 - \mathcal{A}z/z_0} - 1 + \sqrt{1 - \mathcal{A}} \left[ \frac{1}{2} \ln \left( \frac{\sqrt{1 - \mathcal{A}} + 1}{\sqrt{1 - \mathcal{A}} - 1} \right) + \arctan \sqrt{\frac{1 + \mathcal{A}z/z_0}{\mathcal{A} - 1}} \right]. \end{aligned} \quad (2.27)$$

These vertical velocity profiles are displayed in figure 2(b) for different values of  $\mathcal{A}$ . The logarithmic case  $u_x/u_b = \kappa^{-1} \ln(1 + z/z_0)$  is recovered for  $\mathcal{A} = 0$ . Interestingly, this family of profiles allows for the possibility of recirculation when  $\mathcal{A}$  is negative, i.e. for a velocity which changes its sign. In practice, horizontal variations of pressure and shear stress are generated by the presence of a bump. For example, as the velocity is larger at the crests than in the troughs, there is a pressure gradient which is negative on the stoss side and positive on the lee side of the bump. The separation of streamlines and the formation of a recirculation bubble are commonly observed on the lee side of obstacles, which is consistent with a negative value of  $\mathcal{A}$  as the back flow corresponds to  $u_b < 0$ . Field measures have already evidenced that the vertical velocity profiles along dune surfaces is not well fitted by the logarithmic law (?). In particular, this makes difficult the estimate of the basal shear stress from the average velocity profiles. Our result suggests a simple way to overcome this problem by decomposing the flow field into a succession of profiles parametrised by the basal shear velocity  $u_b(x)$  *but also by the dimensionless number*  $\mathcal{A}(x)$ .

### 3. Unbounded turbulent boundary layer over a wavy bottom

We now consider the turbulent flow over a wavy bottom constituting the floor of an unbounded boundary layer. In rivers, this corresponds to the limit of a flow depth  $H$  much larger than the bed-form wavelength  $\lambda$ . The solution is computed as a first order linear correction to the flow over a uniform bottom, using the second order turbulent closure previously introduced.

#### 3.1. Linearised equations

For small enough amplitudes, we can consider a bottom profile of the form  $Z(x) = \zeta \cos(kx)$  without loss of generality.  $\lambda = 2\pi/k$  is the wavelength of the bottom and  $\zeta$  the amplitude of the corrugation, see figure 1. The case of an arbitrary relief can be deduced by a simple superposition of Fourier modes. We introduce the dimensionless variable

$\eta = kz$ , the dimensionless roughness  $\eta_0 = kz_0$  and the function:

$$\mu(\eta) = \frac{1}{\kappa} \ln \left( 1 + \frac{\eta}{\eta_0} \right) \quad (3.1)$$

We also switch to the standard complex number notation:  $Z(x) = \zeta e^{ikx}$  (real parts of expressions are understood).

We wish to perform the linear expansion of equations (2.10)-(2.17) with respect to the small parameter  $k\zeta$ . The mixing length is still defined as the geometrical distance to the bottom:  $L = z_0 + z - Z$ . We introduce the following notations for the first two orders:

$$u_x = u_* [\mu + k\zeta e^{ikx} U], \quad (3.2)$$

$$u_z = u_* k\zeta e^{ikx} W, \quad (3.3)$$

$$\tau_{xz} = \tau_{zx} = -u_*^2 [1 + k\zeta e^{ikx} S_t], \quad (3.4)$$

$$p + \tau_{zz} = p_0 + u_*^2 \left[ \frac{1}{3} \chi^2 + k\zeta e^{ikx} S_n \right], \quad (3.5)$$

$$\tau_{zz} = u_*^2 \left[ \frac{1}{3} \chi^2 + k\zeta e^{ikx} S_{zz} \right], \quad (3.6)$$

$$\tau_{xx} = u_*^2 \left[ \frac{1}{3} \chi^2 + k\zeta e^{ikx} S_{xx} \right]. \quad (3.7)$$

The quantities  $U$ ,  $W$ , etc, are implicitly considered as functions of  $\eta$ . An alternative choice is to consider functions of the coordinate  $\xi = \eta - kZ$ . Such alternative functions are denoted with a tilde to make the distinction. This important – but somehow technical – issue of the choice of a representation is discussed in appendix A. Although the curvilinear and Cartesian systems of coordinates are equivalent, the distinction between the two is of importance when it comes to the expression of the boundary conditions, and for the range of amplitudes  $\zeta$  for which the linear analysis is no more valid (see section 4). In particular, vertical profiles in the forthcoming figures will be mostly plotted as a function of the shifted variable  $\xi$ .

The linearised strain rate tensor reads

$$\dot{\gamma}_{xz} = \dot{\gamma}_{zx} = ku_* \mu' + u_* k^2 \zeta e^{ikx} (U' + iW), \quad (3.8)$$

$$\dot{\gamma}_{xx} = 2iu_* k^2 ZU, \quad (3.9)$$

$$\dot{\gamma}_{zz} = 2u_* k^2 ZW', \quad (3.10)$$

$$|\dot{\gamma}| = |\dot{\gamma}_{xz}|, \quad (3.11)$$

and the stress relaxation equations can be simplified into

$$(\mu' + i\beta\mu)S_t = 2(U' + iW) - 2\kappa^2(\eta + \eta_0)\mu'^3, \quad (3.12)$$

$$(\mu' + i\beta\mu)S_{xx} = -2iU + \frac{2}{3}\chi^2(U' + iW) - \frac{2}{3}\chi^2\kappa\mu'^2, \quad (3.13)$$

$$(\mu' + i\beta\mu)S_{zz} = -2W' + \frac{2}{3}\chi^2(U' + iW) - \frac{2}{3}\chi^2\kappa\mu'^2. \quad (3.14)$$

Finally the Navier-Stokes equations lead to

$$W' = -iU, \quad (3.15)$$

$$S_t' = \mu iU + \mu' W + iS_n + iS_{xx} - iS_{zz}, \quad (3.16)$$

$$S_n' = -\mu iW + iS_t. \quad (3.17)$$

Taking the difference of equations (3.13) and (3.14), one can compute

$$S_{zz} - S_{xx} = \frac{4iU}{\mu' + i\beta\mu} \quad (3.18)$$

to obtain four closed equations:

$$U' = -iW + \frac{\mu' + i\beta\mu}{2} S_t + \kappa\mu'^2, \quad (3.19)$$

$$W' = -iU, \quad (3.20)$$

$$S_t' = \left( i\mu + \frac{4}{\mu' + i\beta\mu} \right) U + \mu'W + iS_n, \quad (3.21)$$

$$S_n' = -i\mu W + iS_t. \quad (3.22)$$

$$(3.23)$$

Introducing the vector  $\vec{X} = (U, W, S_t, S_n)$ , we finally get at the first order in  $k\zeta$  the following compact form of the equation to integrate:

$$\frac{d}{d\eta} \vec{X} = \mathcal{P} \vec{X} + \vec{S}, \quad \text{with } \mathcal{P} = \begin{pmatrix} 0 & -i & \frac{\mu' + i\beta\mu}{2} & 0 \\ -i & 0 & 0 & 0 \\ \left( i\mu + \frac{4}{\mu' + i\beta\mu} \right) & \mu' & 0 & i \\ 0 & -\mu i & i & 0 \end{pmatrix} \quad \text{and } \vec{S} = \begin{pmatrix} \kappa\mu'^2 \\ 0 \\ 0 \\ 0 \end{pmatrix}. \quad (3.24)$$

### 3.2. Resolution of the linearised equations

Four boundary conditions must be specified to solve equation (3.24): two on the ground and two at infinity. Concerning the upper boundary condition, we impose that the vertical fluxes of matter and momentum should vanish asymptotically. This means that, for  $z \rightarrow \infty$ , the first order corrections to the shear stress and to the vertical velocity must tend to zero:  $W(\infty) = 0$  and  $S_t(\infty) = 0$ . On the bottom, we require that both components of the velocity vanish. This leads to  $W(0) = 0$  and  $U(0) = -\mu'(0) = -1/(\kappa\eta_0)$ .

The solution is a linear superposition of a particular solution  $\vec{X}_s$  and the two general solutions  $\vec{X}_t$  and  $\vec{X}_n$  defined by:

$$\frac{d}{d\eta} \vec{X}_s = \mathcal{P} \vec{X}_s + \vec{S} \quad \text{with} \quad \vec{X}_s(0) = \begin{pmatrix} -1/(\kappa\eta_0) \\ 0 \\ 0 \\ 0 \end{pmatrix}, \quad (3.25)$$

$$\frac{d}{d\eta} \vec{X}_t = \mathcal{P} \vec{X}_t \quad \text{with} \quad \vec{X}_t(0) = \begin{pmatrix} 0 \\ 0 \\ 1 \\ 0 \end{pmatrix}, \quad (3.26)$$

$$\frac{d}{d\eta} \vec{X}_n = \mathcal{P} \vec{X}_n \quad \text{with} \quad \vec{X}_n(0) = \begin{pmatrix} 0 \\ 0 \\ 0 \\ 1 \end{pmatrix}. \quad (3.27)$$

Writing the solution under the form  $\vec{X} = \vec{X}_s + a_t \vec{X}_t + a_n \vec{X}_n$ , the boundary conditions on the bottom are automatically verified, and the top ones are encoded into algebraic equations on the real and imaginary parts of  $a_t$  and  $a_n$ . In practice, the equations are solved using a fourth order Runge-Kutta method. A boundary at finite height  $H$  (at

$\eta_H = kH$ ) is introduced at which we impose a null tangential stress  $S_t(\eta_H) = 0$  and vertical velocity  $W(\eta_H) = 0$ . Then, we consider the limit  $H \rightarrow +\infty$ , i.e. when the results become independent of  $H$ .

### 3.3. Alternative boundary conditions

This derivation presents two important limits. The first is practical and concerns its numerical cost: indeed, one needs to resolve the inner length scale  $z_0$  even for very large values of  $\lambda/z_0$ . The second is physical: the expression  $\ln(1 + z/z_0)$  is convenient but is an accurate description of real flows only far from the boundary. This suggests to perform an asymptotic matching between the physics valid at the scale  $z_0$  and that valid at the scale  $\lambda$ . In the limit  $\eta_0 \rightarrow 0$ , one can expand the solution of equation (3.24) in powers of  $\eta$  and  $\ln \frac{\eta}{\eta_0}$ . For this purpose, one can make use of the surface layer approximation developed in the previous section, replacing the variable  $z$  by the actual distance to the bottom  $z - Z$ . The limit of small  $\eta_0$  corresponds to  $z - Z \gg z_0$ , and the linearity condition is satisfied if  $|\mathcal{A}|(z - Z) \ll z_0$ . Under these assumptions, the velocity profile (2.24) is expressed at the first order as

$$u_x \sim \frac{u_b}{\kappa} \left( \frac{\mathcal{A}(\eta - kZ)}{2\eta_0} + \ln \frac{\eta - kZ}{\eta_0} \right) = \frac{u_b}{\kappa} \ln \frac{\eta - kZ}{\eta_0} + \frac{\partial_x \wp}{2\kappa k |u_b|} (\eta - kZ). \quad (3.28)$$

In terms of  $S_t$  and  $S_n$ , we express  $u_b$  and  $\partial_x \wp$  as

$$u_b^2 = u_*^2 [1 + k\zeta e^{ikx} S_t(0)] \quad \text{and} \quad \partial_x \wp = i u_*^2 k^2 \zeta e^{ikx} S_n(0), \quad (3.29)$$

so that  $u_x$  reads

$$u_x = u_* \left[ \mu(\eta) + k\zeta e^{ikx} \left( \frac{S_t(0)}{2} \mu(\eta) - \frac{1}{\kappa \eta} + \frac{i S_n(0)}{\kappa} \eta \right) \right], \quad (3.30)$$

where

$$\mu(\eta) \sim \frac{1}{\kappa} \ln \frac{\eta}{\eta_0} \quad \text{and} \quad \mu'(\eta) \sim \frac{1}{\kappa \eta}. \quad (3.31)$$

corresponds to the function given in (3.1) in the limit  $\eta_0 \ll \eta$ . Altogether we finally get the following expression of the modes:

$$U(\eta) = \frac{S_t(0)}{2\kappa} \ln \frac{\eta}{\eta_0} + \frac{i S_n(0)}{2\kappa} \eta - \frac{1}{\kappa \eta}, \quad (3.32)$$

$$W(\eta) = -\frac{i S_t(0)}{2\kappa} \eta \left( \ln \frac{\eta}{\eta_0} - 1 \right) + \frac{S_n(0)}{4\kappa} \eta^2 + \frac{i}{\kappa} \ln \frac{\eta}{\eta_0}, \quad (3.33)$$

$$S_t(\eta) = S_t(0) + i S_n(0) \eta, \quad (3.34)$$

$$S_n(\eta) = S_n(0) \quad (3.35)$$

In this limit, the general solution of the linear equations (3.24) can be decomposed over four modes:

$$\vec{X} \underset{\eta \rightarrow 0}{\sim} a_1 \begin{pmatrix} \mu^2/4 \\ 1 \\ \mu \\ -\eta^2 \mu^3/4 \end{pmatrix} + a_2 \begin{pmatrix} \mu/2 \\ -i \eta \mu/2 \\ 1 \\ i \eta \end{pmatrix} + a_3 \begin{pmatrix} 1 \\ -i \eta \\ i \eta \mu(\eta) \\ -\eta^2 \mu(\eta) \end{pmatrix} + a_4 \begin{pmatrix} i \eta / (2\kappa) \\ \eta^2 / (4\kappa) \\ i \eta \\ 1 \end{pmatrix} + \vec{X}_s, \quad (3.36)$$

where  $\vec{X}_s$  is the particular solution of equation (3.25). The next terms in this expansion are  $\mathcal{O}(\eta \ln^2 \frac{\eta}{\eta_0})$ , which means that these expressions are excellent as soon as  $\eta$  is smaller than 1, whatever the value of  $\eta_0$ .

The alternative boundary condition thus corresponds to a selection of two of the four

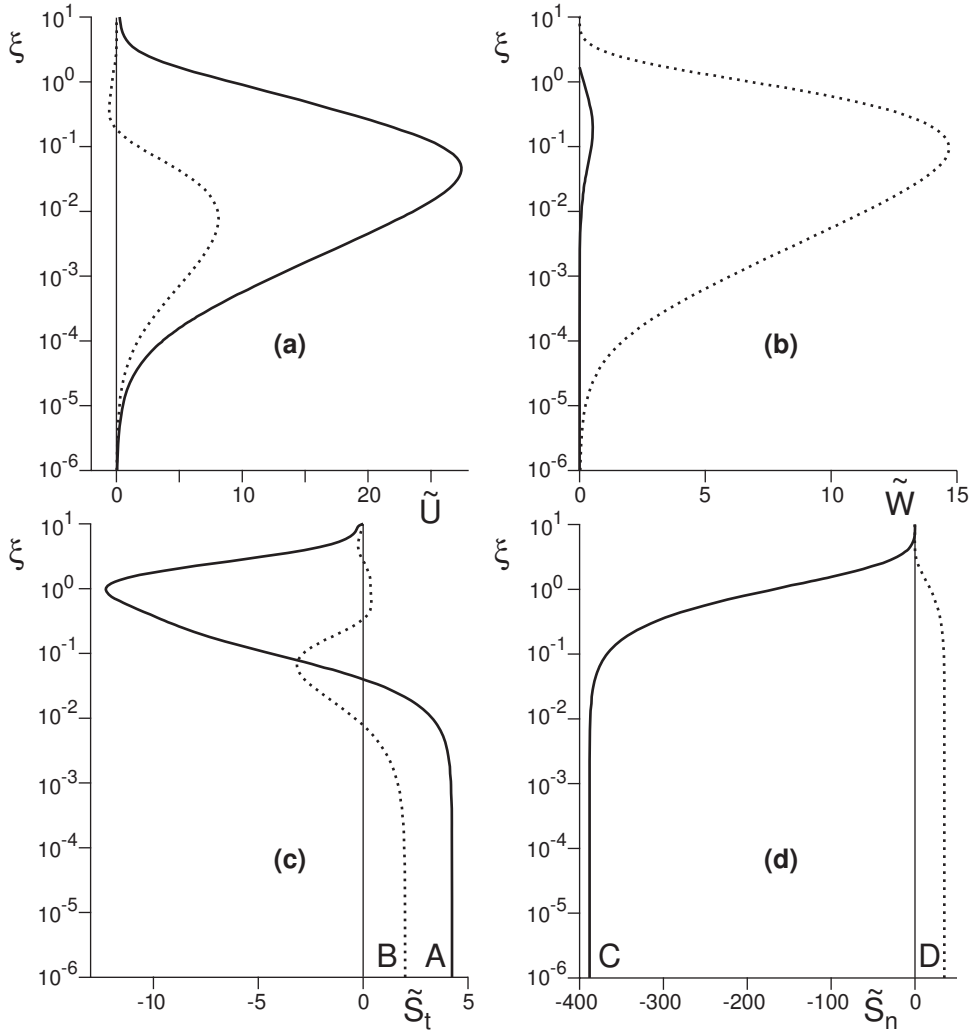


FIGURE 3. Vertical profiles of the first order corrections to velocities and stresses for  $\eta_0 = 10^{-4}$  and  $\beta = 0$ .  $\xi = \eta - kZ$  is the distance to the soil rescaled by the wavenumber. In all panels, the solid lines represent the real parts of the functions, whereas the dashed lines represent the imaginary ones. We note  $\tilde{S}_t(0) = A + iB$  and  $\tilde{S}_n(0) = C + iD$ . Close to the boundary, for  $\xi < 10^{-2}$ , a zone of constant shear stress can be observed, which corresponds to the logarithmic zone. It is embedded into a larger layer of constant pressure ( $\xi < 10^{-1}$ ) in which the shear stress varies linearly. Above this layer, all quantities decrease over one wavelength.

asymptotic behaviours:  $a_1 = 0$ ,  $a_2 = S_t(0)$ ,  $a_3 = 0$  and  $a_4 = S_n(0)$ . It allows to solve the two problems risen above. First, in the limit of small  $\eta_0$ , these asymptotic expansions leads accurately to the same solutions and can be used to speed up the numerical integration of (3.24). As a matter of fact, one can start the Runge-Kutta algorithm at an initial value of  $\eta$  much larger than  $\eta_0$  (it should verify  $\eta \ln^2 \frac{\eta}{\eta_0} \ll 1$ ). Second, it is important to compare the solutions obtained with one or the other boundary condition. In the range of parameters for which they collapse, the details of the processes responsible for the hydrodynamic roughness can be safely ignored.

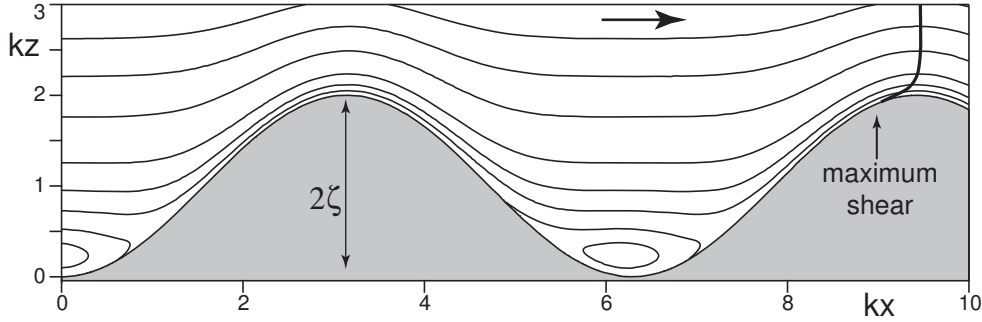


FIGURE 4. Flow streamlines above a wavy bottom (see appendix ??). The flow direction is from left to right. Note the left-right asymmetry of the streamlines around the bump and the presence of a recirculation in the trough. The thick line in the top right corner shows the positions that maximises the velocity along a streamline.

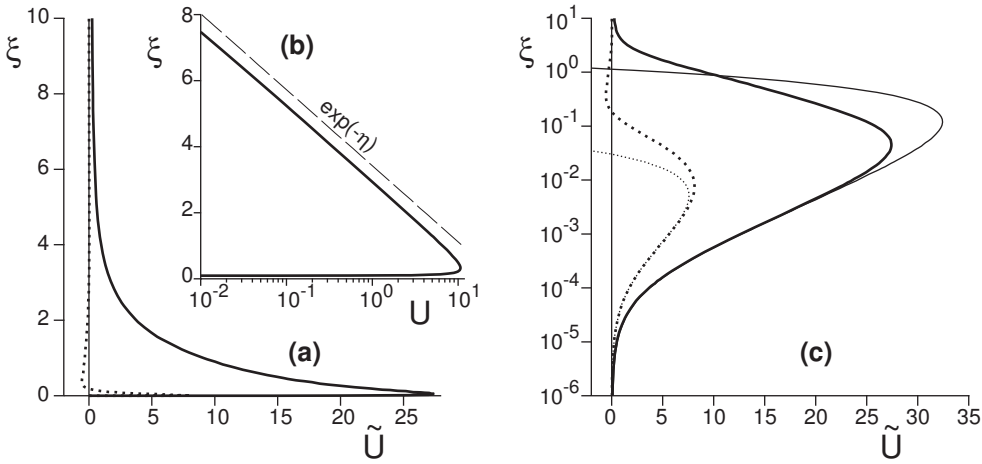


FIGURE 5. Vertical profiles of the first order correction to the horizontal velocity for  $\eta_0 = 10^{-4}$  and  $\beta = 0$ . The solid lines correspond to the real part and the dashed line to the imaginary one. (a) and (b) focus on the upper region, where the behaviour of the flow is that of a potential flow (exponential decrease, long dashed line). The frictional boundary layer above the bottom is shown in the semi-logarithmic plot (c). The thin lines represent the boundary layer approximation close to the bottom: the frictional layer extends roughly up to  $\eta = 10^{-2}$ .

### 3.4. Results

The velocity and stress profiles resulting from the integration of equation (3.24) are displayed in figure 3 for the case  $\beta = 0$ . Looking at panels (c) and (d), one can see a region close to the bottom where the stresses remain constant. These plateaus correspond to a boundary layer in which the flow is locally that of a uniform bottom, as computed above. Away from the bottom, all profiles tend to zero, so that one recovers the undisturbed flow field (2.3). The shape of these modes are very consistent with the work of ?, which means that the precise choice of the turbulent closure is only quantitatively important.

In order to visualize the effect of the bottom corrugation on the flow, the flow streamlines are displayed in figure 4 (see appendix ?? for explanations about their computation). It can be observed that the velocity gradient is larger on the crest than in the troughs as the streamlines are closer to each other. The flow is disturbed over a vertical distance comparable to the wavelength. A more subtle piece of information concerns the position

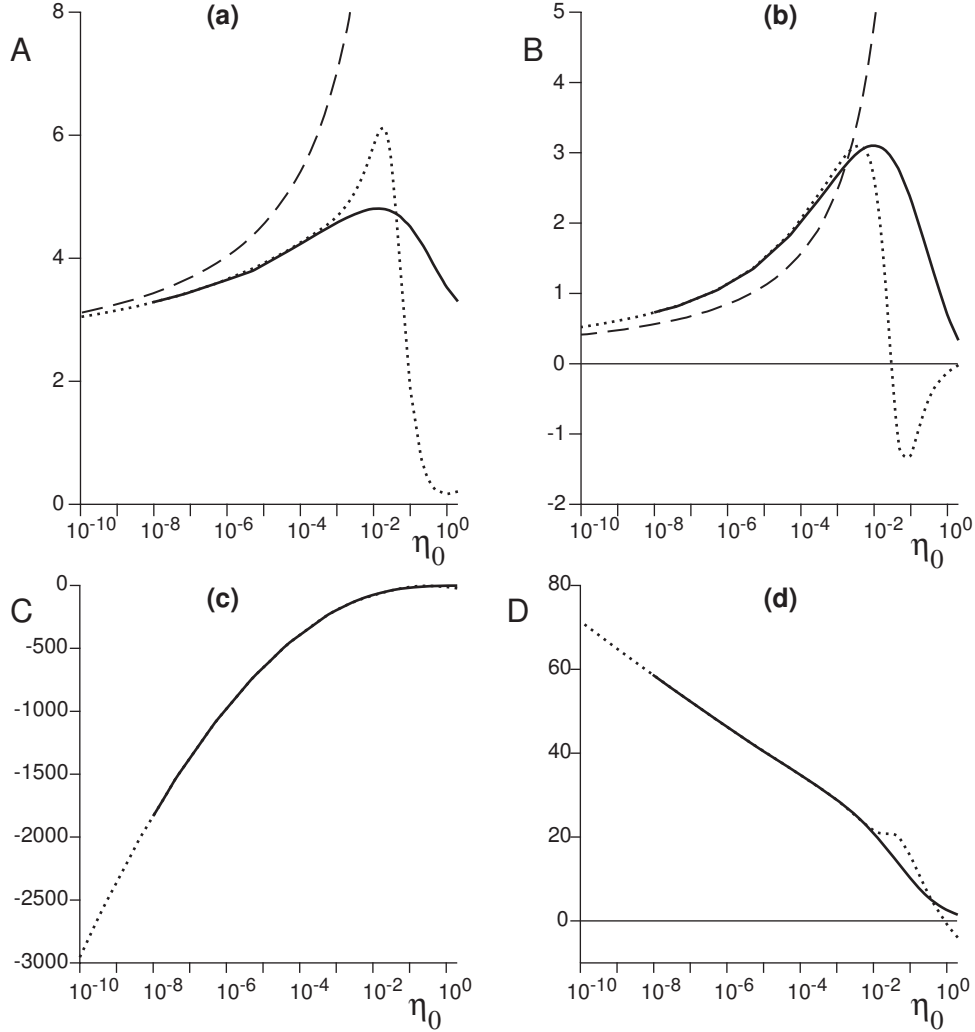


FIGURE 6. Coefficients  $A$ ,  $B$ ,  $C$  and  $D$  as a function of  $\eta_0 = kz_0$ . These plots show the dependence of the basal shear and normal stresses with the number of decades separating the wavelength  $\lambda$  from the soil roughness  $z_0$ , for a given bump aspect ratio. The solid line corresponds to the regularised base flow  $\mu = \kappa^{-1} \ln(1 + \eta/\eta_0)$  and the dotted line to the asymptotic matching with the surface layer (i.e. to  $\mu = \kappa^{-1} \ln(\eta/\eta_0)$ ). The results are very close to each other for  $\eta_0 < 10^{-2}$ . The dashed lines represent the analytical formula deduced from Jackson & Hunt work (Jackson & Hunt 1975, Kroy & al. 2002). They all agree well at very small  $\eta_0$ .

along each streamline at which the velocity is maximum. These points are displayed on the right corner of figure 4. Away from the bottom, they are aligned above the crest of the bump. Very close to it, however, they are shifted upstream. In other words, the fluid velocity is in phase with the bottom in the upper part of the flow, but not in the surface layer where the basal shear stress is exerted. This asymmetry of the flow can be also seen, comparing the streamlines up and down stream the bump: they are closer to each other on the stoss face.

An inspection of the velocity profile evidences two distinct regions (see figure 5(a)-(c)). First there is a region above the bottom ( $\eta > 10^{-1}$ ), where the profile decreases

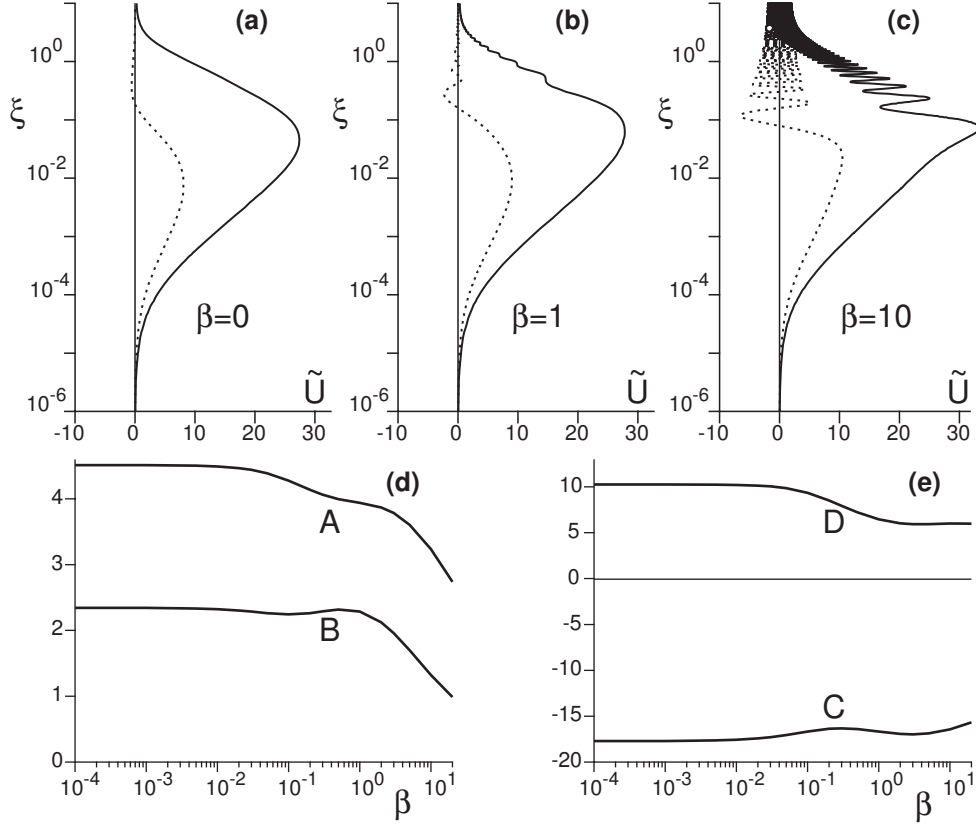


FIGURE 7. Effect of the parameter  $\beta$  on the vertical profiles, here exemplified with the horizontal component of the velocity  $\tilde{U} = U + \mu'$  for  $\eta_0 = 10^{-4}$ .  $\beta$  is a non dimensional parameter encoding the time lag between a change in the strain rate and that of the Reynolds stress. The three panels (a), (b) and (c) are for  $\beta = 0$ ,  $\beta = 1$  and  $\beta = 10$  respectively. One can see that the profiles develop oscillations as  $\beta$  increases, but that the behaviour close to the bottom (in log scale) remains the same. In panels (d) and (e), we plot the coefficients  $A$ ,  $B$ ,  $C$  and  $D$  vs  $\beta$  (still for  $\eta_0 = 10^{-4}$ ). They are weakly affected, meaning again that the behaviour close to the bottom is almost unchanged.

exponentially with  $\eta$  (figure 5(b)). Seeking for asymptotic solutions decreasing as  $e^{-\sigma\eta}$ , one has to solve the eigenvalue problem  $\mathcal{P}\vec{X} = -\sigma\vec{X}$  for asymptotically large values of  $\eta$ . At the two leading orders, the decrease rate  $\sigma$  is given by:

$$2i(\sigma^4 + 1)\eta k^2 + (\sigma^2 - 1)\ln\frac{\eta}{\eta_0} = 0. \quad (3.37)$$

The asymptotic behaviour is an oscillatory relaxation corresponding to  $\sigma = (1 \pm i)/\sqrt{2}$ . However, the observed decrease corresponds to the intermediate asymptotic regime  $\eta < \ln\frac{\eta}{\eta_0}$  for which the solution is  $\sigma = 1$ . This behaviour is reminiscent from that of a potential flow.

In contrast, very close to the bottom, the profile matches very well the asymptotic expression (3.32) computed in the frictional surface boundary layer approximation (thin lines in figure 5(c)). This zone is responsible for the asymmetry of the flow as well as the upstream shift of the maximum velocity discussed above. Let us emphasize again that this is the physical key point for the formation of dunes. One can understand the

reason of the phase shift with the following qualitative argument. Consider the perfect flow around a symmetric bump. The streamlines are symmetrical too, as the flow is solely controlled by the balance between inertia and the pressure gradient induced by the presence of the bump. As a consequence, the velocity is maximum at the crest. Now, inside the frictional layer close to the bottom, this flow must be slowed down. Due to inertia, the velocity needs some time to re-adapt to a change of shear stress. Thus, the shear stress is always phase-advanced with respect to the velocity. Focusing on the region of matching between the external and surface layers, one concludes that the shear stress is phase-advanced with respect to the bump. This can be rephrased from a geometrical point of view. The stream function measures the flow discharge between the floor and a given height. As the frictional surface layer is introduced, the streamlines computed for a perfect flow must be moved up in response to the slowing down of the fluid. Because this process is more pronounced for a larger stress, and taking into account the inertia of the fluid, the streamlines must be moved up more downstream the crest than upstream. As a result, the point at which the streamlines are squeezed the most is shifted upstream.

As mentioned in the introduction, we are especially interested in the shear stress and pressure distributions on the bottom. We note  $\tilde{S}_t(0) = A + iB$  and  $\tilde{S}_n(0) = C + iD$ . The upstream shift of the basal shear stress with respect to the bottom profile then corresponds to a positive coefficient  $B$ . The four coefficients  $A$ ,  $B$ ,  $C$  and  $D$  are displayed as a function of  $\eta_0$  in figure 6. Their overall dependence with  $\eta_0$  is weak, meaning that the turbulent flow around an obstacle is mostly scale invariant. More precisely, following Jackson & Hunt's work (Jackson & Hunt 1975, Kroy & al. 2002), it has been shown that, for asymptotically small  $\eta_0$ , one expects logarithmic dependencies:

$$A = \frac{\ln(\phi^2/\ln\phi)^2}{2(\ln\phi)^3} \left(1 + \ln\phi + 2\ln\frac{\pi}{2} + 4\gamma_E\right) \quad \text{and} \quad B = \pi \frac{\ln(\phi^2/\ln\phi)^2}{2(\ln\phi)^3}, \quad (3.38)$$

where Euler's constant is  $\gamma_E \simeq 0.577$ ,  $\phi$  is defined by the equation  $\phi \ln\phi = 2\kappa^2\Phi$  and with  $\Phi = \pi/(2\eta_0)$ . Note that  $A$  tends to 2 at  $\eta_0 = 0$ , as expected from a simple Bernoulli argument. These expressions agree well with our numerical results for very small  $\eta_0$ . For realistic values of  $\eta_0$  however, e.g.  $10^{-4} < \eta_0 < 10^{-2}$ , this approximation cannot be accurately used as it leads to errors of order one – note that Jackson & Hunt expressions tend to diverge. For  $\eta_0 < 10^{-3}$ , the results are fairly robust with respect to the physics at the scale of  $z_0$ . Indeed, the curves obtained starting from a base flow of the form  $\mu = \kappa^{-1} \ln(1 + \eta/\eta_0)$  and  $\mu = \kappa^{-1} \ln(\eta/\eta_0)$  are close to each other. However, one sees significant differences for  $\eta_0 > 10^{-2}$ .

The normal stress coefficients  $C$  and  $D$  are much more robust to the details of the model. In the limit of a perfect flow, the pressure varies as the square of the velocity. Here, one needs to consider the velocity at the scale  $\lambda$  of the perturbation, say  $u_*\mu$ , where the logarithmic factor  $\mu$  should be evaluated for  $\eta$  of order unity. From this, we predict that the pressure coefficient  $C$  should scale as the square of  $\ln\eta_0$  (a parabola in figure 6), which is very accurately verified. More precisely,  $C = [\mu(1/4)]^2$  is an almost perfect approximation. Finally, it can be observed that the normal stress is also phase-shifted upstream with respect to the bottom profile. The coefficient  $D$  is positive and found to vary linearly with  $\ln\eta_0$ .

Lastly in figure 7, we show the effect of the parameter  $\beta$ . We recall that  $\beta$  encodes the time lag between an increase of the mean shear strain rate and the corresponding readjustment of the fluctuations of the shear stress. From dimensional analysis, we expect  $\beta$  to be of order one. As expected for inertial effects in a relaxation process, finite values of  $\beta$  generate oscillations in the vertical profiles of the velocities and stresses. The example

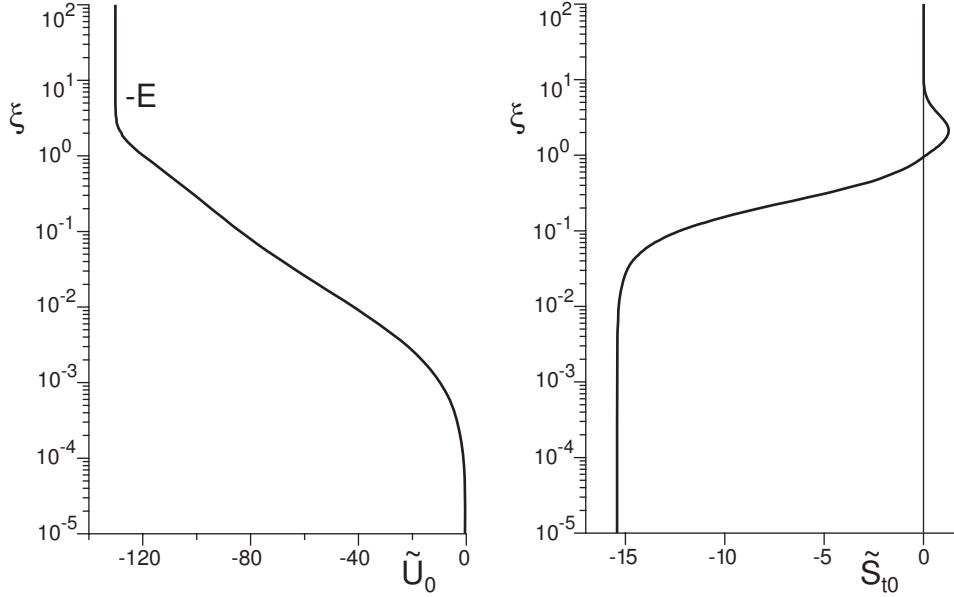


FIGURE 8. Vertical profiles of the homogeneous second order corrections  $\tilde{U}_0$  (a) and  $\tilde{S}_{t0}$  (b). These curves have been computed with  $\eta_0 = 2 \cdot 10^{-3}$ .  $\tilde{U}_0$  tends towards a negative constant value  $-E$  at large  $\zeta$ . Notice also that, close to the bottom,  $\tilde{S}_{t0}$  has a constant value, reminiscent of the surface boundary layer.

of the horizontal velocity is displayed in the panels (a), (b) and (c). The amplitude and the frequency of these oscillations increase with  $\beta$ . Interestingly, these oscillations do not affect much the behaviour of the modes close to the bottom. As a consequence, the coefficients  $A$ ,  $B$ ,  $C$  and  $D$  are weakly affected by  $\beta$ , see panels (d) and (e). As expected, this dynamical mechanism induces a downstream phase shift of the shear stress: the value of  $B$  decreases as  $\beta$  increases.

#### 4. Weakly non-linear expansion

In this section we investigate the non-linear effects at finite values of the bottom corrugation amplitude  $\zeta$ . In particular, we wish to address two issues: first, can one relate the hydrodynamic roughness to geometrical quantities; second, can we aim to describe with a weakly non-linear theory, the separation of streamlines, the formation of a recirculation bubble and their effect on the basal stress coefficients  $A$ ,  $B$ ,  $C$  and  $D$ . These results will be used in the third part of this paper, to determine the equilibrium height of dunes.

##### 4.1. Expansion in amplitude

We perform an expansion with respect to the bottom corrugation amplitude up to  $\zeta^3$  and introduce non-dimensional functions for the different orders:

$$u_x = u_* [\mu + (k\zeta)e^{ikx}U_1 + (k\zeta)^2U_0 + (k\zeta)^2e^{2ikx}U_2 + (k\zeta)^3e^{ikx}U_3], \quad (4.1)$$

$$u_z = u_* [(k\zeta)e^{ikx}W_1 + (k\zeta)^2W_0 + (k\zeta)^2e^{2ikx}W_2 + (k\zeta)^3e^{ikx}W_3], \quad (4.2)$$

$$\tau_{xz} = -u_*^2 [1 + (k\zeta)e^{ikx}S_{t1} + (k\zeta)^2S_{t0} + (k\zeta)^2e^{2ikx}S_{t2} + (k\zeta)^3e^{ikx}S_{t3}], \quad (4.3)$$

$$p + \tau_{zz} = p_0 + u_*^2 [(k\zeta)e^{ikx}S_{n1} + (k\zeta)^2S_{n0} + (k\zeta)^2e^{2ikx}S_{n2} + (k\zeta)^3e^{ikx}S_{n3}], \quad (4.4)$$

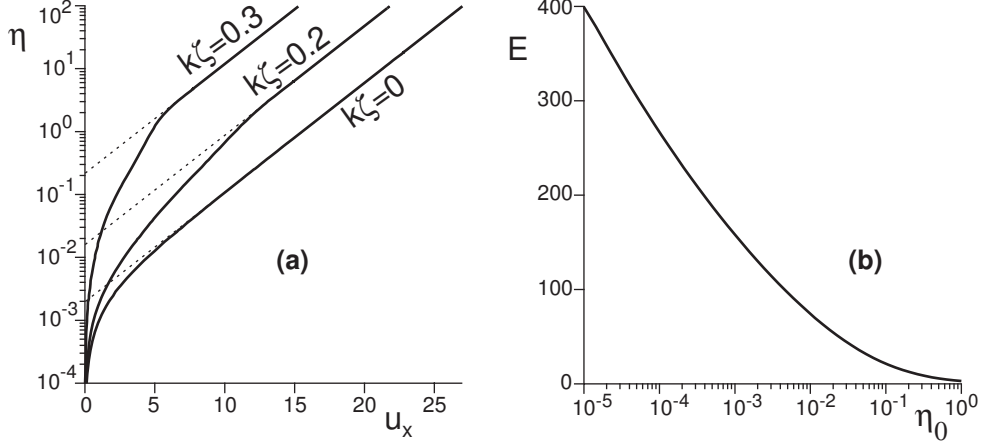


FIGURE 9. (a) Vertical profiles of the homogeneous component of the velocity  $\mu + (k\zeta)^2 \tilde{U}_0$  for  $k\zeta = 0$ ,  $k\zeta = 0.2$  and  $k\zeta = 0.3$ . The extrapolation to 0 of the upper part of the curves gives the value of the apparent roughness  $z_a$ . (b) Coefficient  $E$  as a function of  $\eta_0$ . For a given aspect ratio  $k\zeta$  of the bottom corrugation,  $z_a$  increases with  $E$ . Thus, the apparent roughness gets larger as the separation between the wavelength  $\lambda$  and the bottom roughness  $z_0$  increases.

$$\tau_{zz} - \tau_{xx} = u_*^2 [(k\zeta)e^{ikx} S_{d1} + (k\zeta)^2 S_{d0} + (k\zeta)^2 e^{2ikx} S_{d2} + (k\zeta)^3 e^{ikx} S_{d3}]. \quad (4.5)$$

The non-linear effects result from the expansion of the mixing length (terms in  $(k\zeta)^2$ ) and from the self-interaction of the linear perturbations: in particular, the combination of terms  $(k\zeta)e^{ikx}$  generates second order terms in  $(k\zeta)^2$ . All functions are complex, except  $\mu$  and those related to the second order homogeneous corrections (index 0).

Although the principle of the expansion in amplitude is simple, the actual calculations are painful, and the technical details have been gathered in appendix B. In summary, one obtains a linear hierarchy of linear equations:

$$\frac{d}{d\eta} \vec{X}_\alpha = \mathcal{P}_\alpha \vec{X}_\alpha + \vec{S}_\alpha, \quad (4.6)$$

where  $\vec{X}_\alpha = (U_\alpha, W_\alpha, S_{t\alpha}, S_{n\alpha})$ . Of course,  $\mathcal{P}_1$  and  $\vec{S}_1$  are the matrix and vector of expression (3.24) – for simplicity we set  $\beta = 0$  in this section. We have  $\mathcal{P}_3 = \mathcal{P}_1$ ,  $\mathcal{P}_2$  is slightly different and  $\mathcal{P}_0$  is very simple:

$$\mathcal{P}_1 = \mathcal{P}_3 = \begin{pmatrix} 0 & -i & \frac{\mu'}{2} & 0 \\ -i & 0 & 0 & 0 \\ \left(i\mu + \frac{4}{\mu'}\right) & \mu' & 0 & i \\ 0 & -\mu i & i & 0 \end{pmatrix}, \quad (4.7)$$

$$\mathcal{P}_2 = \begin{pmatrix} 0 & -2i & \frac{\mu'}{2} & 0 \\ -2i & 0 & 0 & 0 \\ 2\left(i\mu + \frac{8}{\mu'}\right) & \mu' & 0 & 2i \\ 0 & -2\mu i & 2i & 0 \end{pmatrix}, \quad \text{and} \quad \mathcal{P}_0 = \begin{pmatrix} 0 & 0 & \frac{\mu'}{2} & 0 \\ 0 & 0 & 0 & 0 \\ 0 & 0 & 0 & 0 \\ 0 & 0 & 0 & 0 \end{pmatrix}. \quad (4.8)$$

All the heaviness of the method is in the expression of the right hand terms  $\vec{S}_\alpha$ : the components of such vectors at a given order depend on the lower order functions  $\vec{X}_\alpha$  and their derivatives. The integration has thus to follow the hierarchy of the equations, one order after the other.

## 4.2. Boundary conditions

Some boundary conditions must be specified in order to perform the integrations. As before, both components of the velocity should vanish on the bottom  $z = Z$ . These conditions express easily in the shifted representation, i.e. written in terms of the curvilinear coordinates (see appendix A): they simply read  $\tilde{U}_\alpha(0) = 0$  and  $\tilde{W}_\alpha(0) = 0$ . In terms of the Cartesian functions, we get:

$$U_1(0) = -\mu'(0), \quad (4.9)$$

$$U_0(0) = -\frac{1}{4}\mu''(0) - \frac{1}{2}\kappa\mu'^2(0) - \frac{1}{8}\mu'(0) [S_{t1}(0) + S_{t1}^*(0)], \quad (4.10)$$

$$U_2(0) = -\frac{1}{4}\mu''(0) - \frac{1}{2}\kappa\mu'^2(0) - \frac{1}{4}\mu'(0)S_{t1}(0), \quad (4.11)$$

$$\begin{aligned} U_3(0) = & -\frac{1}{8}\mu'''(0) + \frac{9}{8}\mu'(0) - \frac{3}{4}\kappa^2\mu'^3(0) - \frac{1}{16} [\mu''(0) + 2\kappa\mu'^2(0)] [2S_{t1}(0) + S_{t1}^*(0)] \\ & + \frac{1}{32}\mu'(0)S_{t1}(0) [S_{t1}(0) + 2S_{t1}^*(0)] - \frac{i}{16}\mu'(0) [2S_{n1}(0) + S_{n1}^*(0)] \\ & - \frac{1}{4}\mu'(0) [2S_{t0}(0) + S_{t2}(0)], \end{aligned} \quad (4.12)$$

and

$$W_1(0) = 0, \quad (4.13)$$

$$W_0(0) = 0, \quad (4.14)$$

$$W_2(0) = -\frac{i}{2}\mu'(0), \quad (4.15)$$

$$W_3(0) = -\frac{i}{4}\mu''(0) - \frac{3i}{8}\kappa\mu'^2(0) - \frac{i}{16}\mu'(0) [2S_{t1}(0) + S_{t1}^*(0)]. \quad (4.16)$$

As in the previous section, for each order, the solution is a linear superposition of the form:  $\vec{X}_\alpha = \vec{X}_{s\alpha} + a_{t\alpha}\vec{X}_{t\alpha} + a_{n\alpha}\vec{X}_{n\alpha}$ , where the different vectors are solutions of the following equations:

$$\frac{d}{d\eta}\vec{X}_{s\alpha} = \mathcal{P}_\alpha\vec{X}_{s\alpha} + \vec{S}_\alpha \quad \text{with} \quad \vec{X}_{s\alpha}(0) = \begin{pmatrix} U_\alpha(0) \\ W_\alpha(0) \\ 0 \\ 0 \end{pmatrix}, \quad (4.17)$$

$$\frac{d}{d\eta}\vec{X}_{t\alpha} = \mathcal{P}_\alpha\vec{X}_{t\alpha} \quad \text{with} \quad \vec{X}_{t\alpha}(0) = \begin{pmatrix} 0 \\ 0 \\ 1 \\ 0 \end{pmatrix}, \quad (4.18)$$

$$\frac{d}{d\eta}\vec{X}_{n\alpha} = \mathcal{P}_\alpha\vec{X}_{n\alpha} \quad \text{with} \quad \vec{X}_{n\alpha}(0) = \begin{pmatrix} 0 \\ 0 \\ 0 \\ 1 \end{pmatrix}. \quad (4.19)$$

For the top boundary conditions, we introduce a lid at finite height  $H$ , impose  $S_{t\alpha}(\eta_H) = 0$  and  $W_\alpha(\eta_H) = 0$ , and look at the limit  $H \rightarrow +\infty$ , i.e. when the results become independent of  $H$ . These conditions lead to two equations on  $a_{t\alpha}$  and  $a_{n\alpha}$ , whose solutions give  $S_{t\alpha}(0)$  and  $S_{n\alpha}(0)$  respectively.

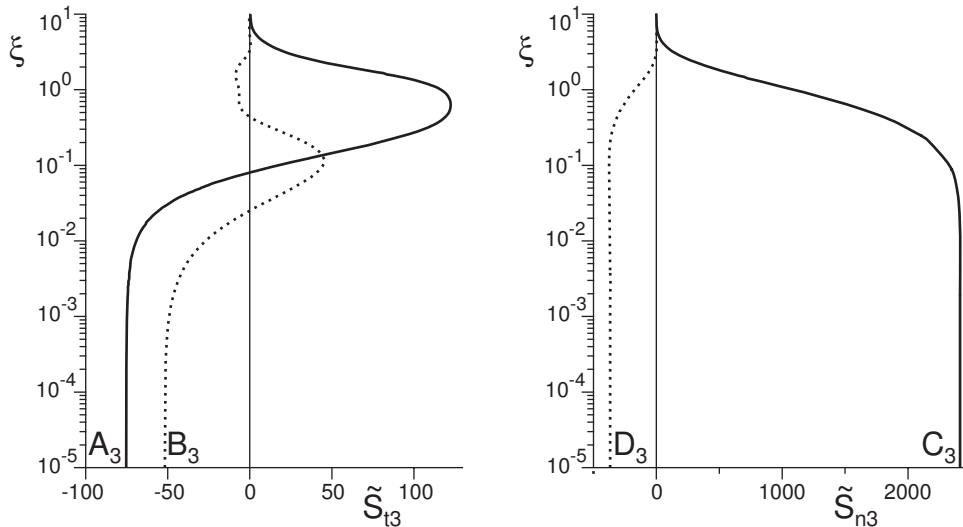


FIGURE 10. Vertical profiles of the third order corrections to the stresses:  $\tilde{S}_{t3}$  (a) and  $\tilde{S}_{n3}$  (b). The solid lines represent the real parts of the functions, whereas the dashed lines represent the imaginary ones. These curves have been computed with  $\eta_0 = 2 \cdot 10^{-3}$ . Notice again the surface boundary layer where the stresses are constant. We note  $\tilde{S}_{t3}(0) = A_3 + iB_3$  and  $\tilde{S}_{n3}(0) = C_3 + iD_3$ . Note that both  $A_3$  and  $B_3$  are negative.

#### 4.3. Results

We first consider the corrections to the homogeneous base solution (index 0). The corresponding velocity profile  $\tilde{U}_0$  and shear stress profile  $\tilde{S}_{t0}$  are displayed in figure 8. The component in  $\zeta^2$  of the velocity decreases continuously from  $z \sim z_0$  to  $z \sim \lambda$  and tends towards a negative constant  $-E$  far from the ground. Correspondingly, the shear stress decreases and tends to 0 far from the ground, as requested. The calculation thus predicts an increase of the turbulent drag (i.e. of the basal shear stress) with the corrugation amplitude, due to the non-linearities. In terms of the velocity profile, this corresponds to an increase of the apparent roughness  $z_a$  of the surface, defined by:

$$u_x \sim \frac{u_*}{\kappa} \ln \frac{z}{z_a}. \quad (4.20)$$

Identifying the expressions far from the ground, we get:

$$\ln z_a \equiv \ln z_0 + \kappa(k\zeta)^2 E, \quad (4.21)$$

As a consequence,  $z_a$  increases with  $E$  and with the aspect ratio  $k\zeta$ . For the seek of illustration, several vertical profiles of the homogeneous part of the velocity  $\mu + (k\zeta)^2 \tilde{U}_0$  are plotted in figure 9(a) for different values of  $k\zeta$ .  $z_a$  is the extrapolation of the asymptotic part of the curves to vanishing velocities. Interestingly, the hydrodynamic roughness  $z_a$  cannot be related to a single geometrical length (e.g. to the corrugation amplitude  $\zeta$ ) only. In particular, we predict that the macroscopic roughness  $z_a$  associated to a wavy surface still depends on the microscopic roughness  $z_0$ : as shown in figure 9(b), for a given aspect ratio, the apparent roughness  $z_a$  gets larger as  $\eta_0$  gets smaller.

The first non-linear corrections to the harmonic terms scale on  $\zeta^3$ . In figure 10, we show the horizontal and vertical stress profiles. As in the first order case, there exists a boundary layer close to the bottom where the stresses are almost constant. As requested, both components vanish far from the ground. We note  $\tilde{S}_{t3}(0) = A_3 + iB_3$  and  $\tilde{S}_{n3}(0) =$

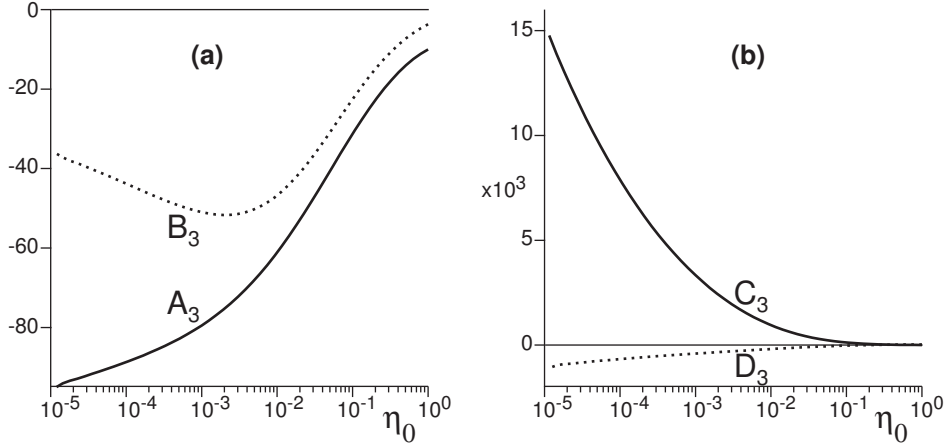


FIGURE 11. Third order stress coefficients  $A_3$ ,  $B_3$ ,  $C_3$  and  $D_3$  as a function  $\eta_0$ . Comparing the signs with those of  $A = A_1$ ,  $B = B_1$ ,  $C = C_1$  and  $D = D_1$ , it can be inferred that the non-linearities oppose the linear effects. In particular, as the amplitude increases, the point of maximum shear stress drifts downstream:  $B + B_3 \zeta^2$  decreases.

$C_3 + iD_3$  the shear and normal stresses acting on the boundary. These coefficients are plotted as a function of  $\eta_0$  in figure 11. Both  $A_3$  and  $B_3$  are negative while  $A = A_1$  and  $B = B_1$  are positive, which means that the first non-linearities oppose the linear effects. We will show in part 3 of this article that this is responsible for the selection of the dune height. Note as from now that the upstream phase shift of the shear stress disappear when  $B + (k\zeta)^2 B_3 = 0$ , when the aspect ratio of relief  $2\zeta/\lambda$  is of the order of  $1/10$ . This corresponds nicely to the aspect ratio of dunes. More generally, whatever the quantity on which the analysis is done, one observes that the non-linearities start playing a role of order one when  $k\zeta$  is of the order of  $1/4$ .

## 5. Effect of a free surface

In this section, we investigate the effect of the additional presence of a free surface at a finite distance  $H$  to the bottom. This situation is relevant for the study of ripples and dunes on the bed of rivers (see part 3 of this article). We follow the outline of the section 3, stay with linear calculations, and keep also to two-dimensional situations.

### 5.1. River equilibrium

In the case of a river inclined at an angle  $\theta$  to the horizontal, the shear stress must balance gravity. It thus varies linearly as  $\tau_{xz} = g(z - H) \sin \theta$  and vanishes at the free surface. By definition of the shear velocity  $u_*$ , we also write  $\tau_{xz} \equiv u_*^2(z/H - 1)$ . In the context of a mixing length approach to describe turbulence, this length should vanish at the free surface. For the sake of simplicity, we take  $L = (z + z_0)\sqrt{1 - z/H}$ . This choice results in a base flow that is logarithmic as in the unbounded situation:

$$u_x = \frac{u_*}{\kappa} \ln \left( 1 + \frac{z}{z_0} \right). \quad (5.1)$$

This is consistent with field and experimental observations. The stress balance equation along the  $z$ -axis allows to get the pressure, which reads:

$$p + \tau_{zz} = p_0 + g(H - z) \cos \theta = p_0 + \frac{u_*^2}{\tan \theta} \left( 1 - \frac{z}{H} \right). \quad (5.2)$$

We define the Froude number as the ratio of the surface velocity to the velocity of gravity surface waves (in the case of a flat bottom):

$$\mathcal{F} \equiv \frac{1}{\sqrt{gH}} \frac{u_*}{\kappa} \ln \left( 1 + \frac{H}{z_0} \right) = \frac{1}{\kappa} \ln \left( 1 + \frac{H}{z_0} \right) \sqrt{\sin \theta}. \quad (5.3)$$

The Froude number can be quite large for sloppy rivers. Take care that  $\mathcal{F}$  is in general small for large natural rivers, as they flow on very small slopes.

### 5.2. Disturbances

In the same manner as in section 3, we consider now a wavy bottom  $Z = \zeta e^{ikx}$ . We note again  $\eta = kz$  and  $\eta_H = kH$ . We write the first order corrections to the base flow as

$$u_x = u_* [\mu + k\zeta e^{ikx} U], \quad (5.4)$$

$$u_z = u_* k\zeta e^{ikx} W, \quad (5.5)$$

$$\tau_{xz} = \tau_{zx} = -u_*^2 \left[ 1 - \frac{\eta}{\eta_H} + k\zeta e^{ikx} S_t \right], \quad (5.6)$$

$$p + \tau_{zz} = p_0 + u_*^2 \left[ \frac{1}{\tan \theta} \left( 1 - \frac{\eta}{\eta_H} \right) + k\zeta e^{ikx} S_n \right], \quad (5.7)$$

where the function  $\mu$  is still defined by the relation (3.1). The free surface is also disturbed and we denote  $H + \Delta(x)$  the flow depth at the position  $x$ . The modified expression for the mixing length then reads

$$L = (z_0 + z - Z) \sqrt{\frac{H + \Delta - z}{H + \Delta - Z}}. \quad (5.8)$$

Linearising the free surface profile as  $\Delta(x) = \delta\zeta e^{ikx}$ , one can expand  $L$  to the first order as

$$kL = (\eta + \eta_0) \sqrt{1 - \frac{\eta}{\eta_H}} \left\{ 1 - k\zeta e^{ikx} \left[ \frac{1}{\eta + \eta_0} - \frac{1}{2\eta_H} - \delta \frac{\eta}{2\eta_H^2 \left( 1 - \frac{\eta}{\eta_H} \right)} \right] \right\}. \quad (5.9)$$

The shear stress relaxation as well as the Navier-Stokes equations can be linearised in the same way as before, and we finally get at the first order in  $Z$  a system of differential equations which can be written under the following form:

$$\frac{d}{d\eta} \vec{X} = \mathcal{P} \vec{X} + \vec{S} + \delta \vec{S}_\delta, \quad (5.10)$$

with

$$\mathcal{P} = \begin{pmatrix} 0 & -i - \frac{\beta}{2\eta_H \left( 1 - \frac{\eta}{\eta_H} \right)} & \frac{\mu' + i\beta\mu}{2 \left( 1 - \frac{\eta}{\eta_H} \right)} & 0 \\ -i & 0 & 0 & 0 \\ \frac{4}{\mu' + i\beta\mu} \left( 1 - \frac{\eta}{\eta_H} \right) + i\mu & \mu' & 0 & i \\ 0 & -\mu i & i & 0 \end{pmatrix}, \quad (5.11)$$

$$\vec{S} = \begin{pmatrix} \kappa\mu'^2 - \frac{\mu'}{2\eta_H} \\ 0 \\ 0 \\ 0 \end{pmatrix}, \quad \text{and} \quad \vec{S}_\delta = \begin{pmatrix} -\frac{\eta\mu'}{2\eta_H^2 \left( 1 - \frac{\eta}{\eta_H} \right)} \\ 0 \\ 0 \\ 0 \end{pmatrix}. \quad (5.12)$$

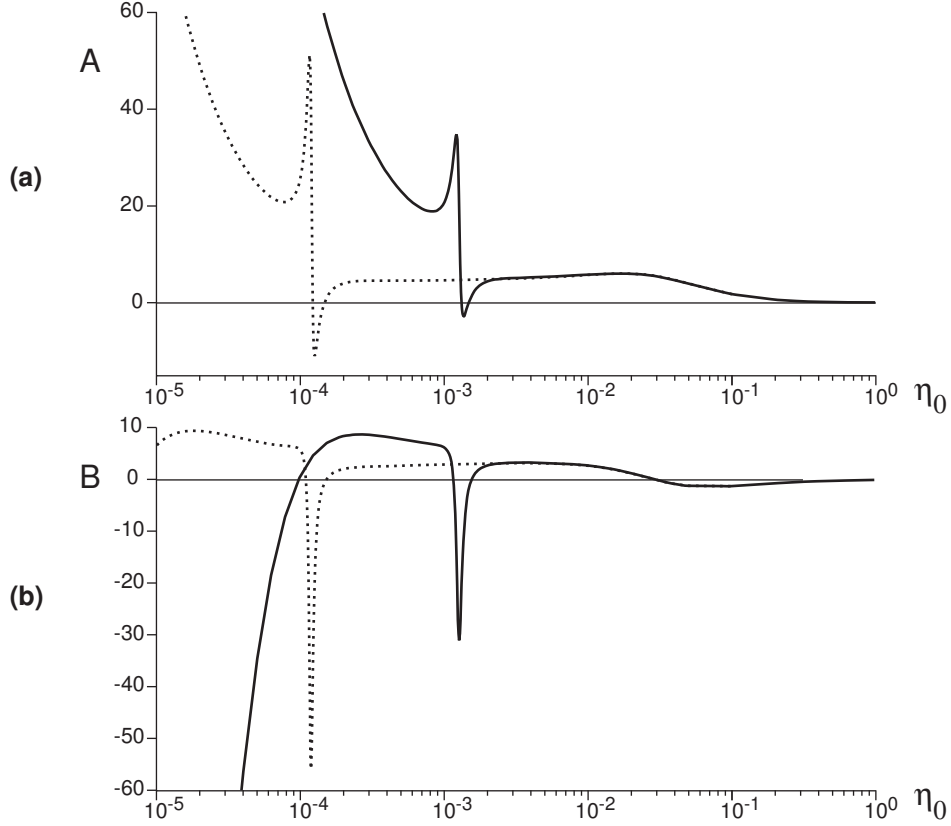


FIGURE 12.  $A$  and  $B$  as functions of  $\eta_0$  for  $\mathcal{F} = 0.9$  and  $H/z_0 = 10^3$  (solid line) or  $H/z_0 = 10^4$  (dotted line). In the right part of the plots, the curves collapse on the shape displayed in panels (a) and (b) of figure 6. They differ at smaller  $\eta_0$ , showing a resonance peak and a divergence at  $\eta_0 \rightarrow 0$ . This graph clearly shows the distinction between the hydrodynamics of ripples, that are not influenced by the free surface, and dunes, dominated by the free surface effect.

### 5.3. Resolution of the linearised equations

Again, making use of the linearity of the equations, we seek the solution under the form  $\vec{X} = \vec{X}_0 + a_t \vec{X}_t + a_n \vec{X}_n + \delta \vec{X}_\delta$ , where the vector  $\vec{X}_\delta$  is solution of equation:

$$\frac{d}{d\eta} \vec{X}_\delta = \mathcal{P} \vec{X}_\delta + \vec{S}_\delta \quad \text{with} \quad \vec{X}_\delta(0) = \begin{pmatrix} 0 \\ 0 \\ 0 \\ 0 \end{pmatrix}, \quad (5.13)$$

while  $\vec{X}_0$ ,  $\vec{X}_t$  and  $\vec{X}_n$  are still solutions of equations (3.25)-(3.27). The bottom boundary conditions  $U(0) = -1/(\kappa\eta_0)$  and  $W(0) = 0$  are then automatically satisfied. At the free surface, we impose the material nature of the surface,  $W(\eta_H) = i\mu(\eta_H)\delta$ , and vanishing stresses:  $S_t(\eta_H) = \delta/\eta_H$  and  $S_n(\eta_H) = \delta/(\eta_H \tan \theta)$ . These last three conditions select the coefficients  $a_t$  and  $a_n$  as well as the value of  $\delta$ . Finally note that the analytical approximation of the solution close to the bottom in the limit  $\eta_0 \rightarrow 0$  is the same as in the unbounded case – it does not depend on the position of the upper boundary – and expressions (3.32)-(3.35) are thus still correct in the limit  $H \gg z_0$ .

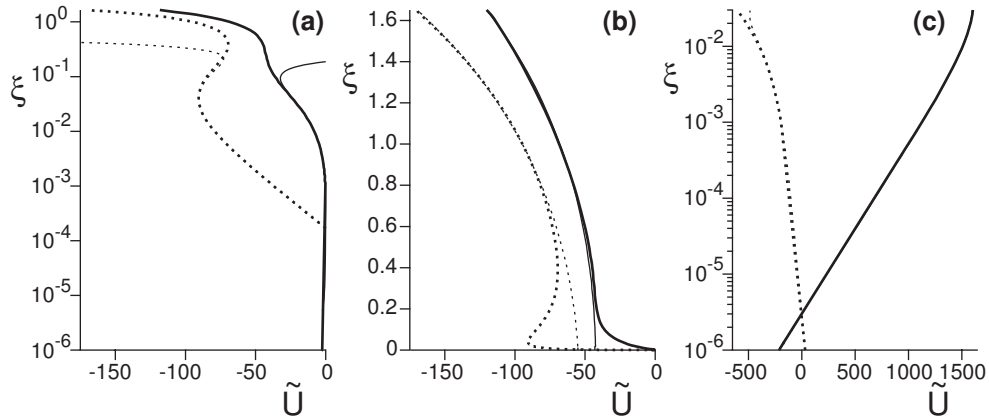


FIGURE 13. Velocity profiles for  $kH = 1.65$  (a)-(b), and  $kH = 0.03$  (c), with  $H/z_0 = 10^4$ . The solid lines represent the real part of the modes, and the dotted lines the imaginary ones. (a) and (b) show the very same profile, but with a logarithmic scale in (a) to emphasize the region close to the bottom. The thin lines in (a) and (c) represent the asymptotic surface layer approximation. Those in (b) correspond to a sum of an increasing and a decreasing exponential of the form  $\exp(\pm\eta)$  (as for a potential flow).

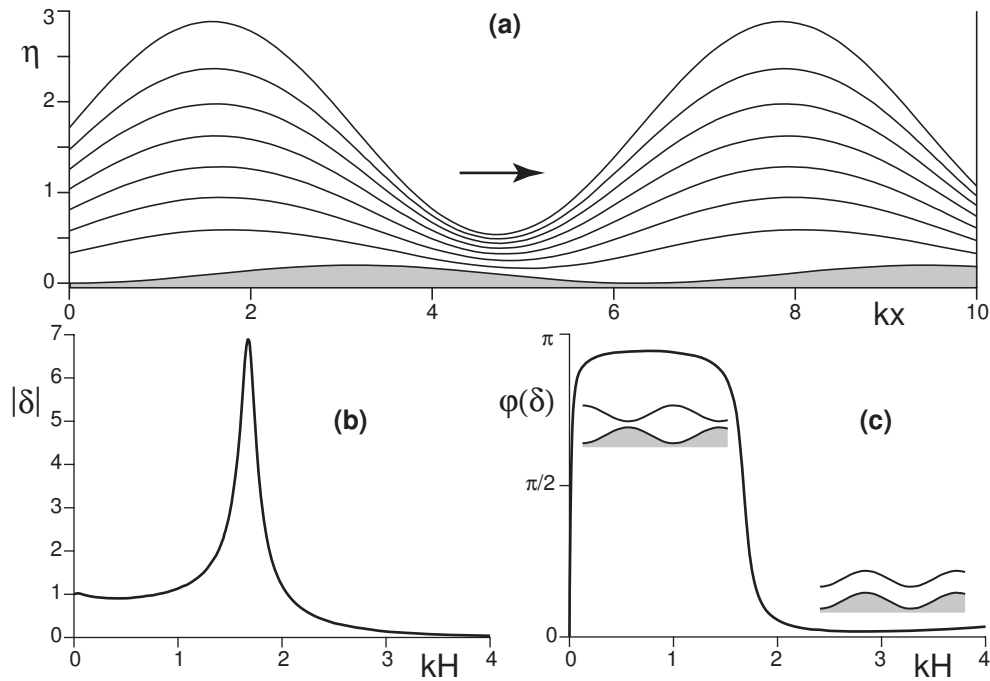


FIGURE 14. (a) Streamlines of a flow over a sinusoidal bottom close to the free surface resonance conditions ( $\varphi = \pi/2$ ). The flow is from left to right. Note the squeezing of the lines *downstream* the crest of the bump. Amplitude (b) and phase (c) of the free surface as a function of  $kH$  for  $\mathcal{F} = 0.8$ . The peak in amplitude and the phase shift from 0 to  $\pi$  correspond to the resonance. The two schematics illustrate the situations in phase or in phase opposition.

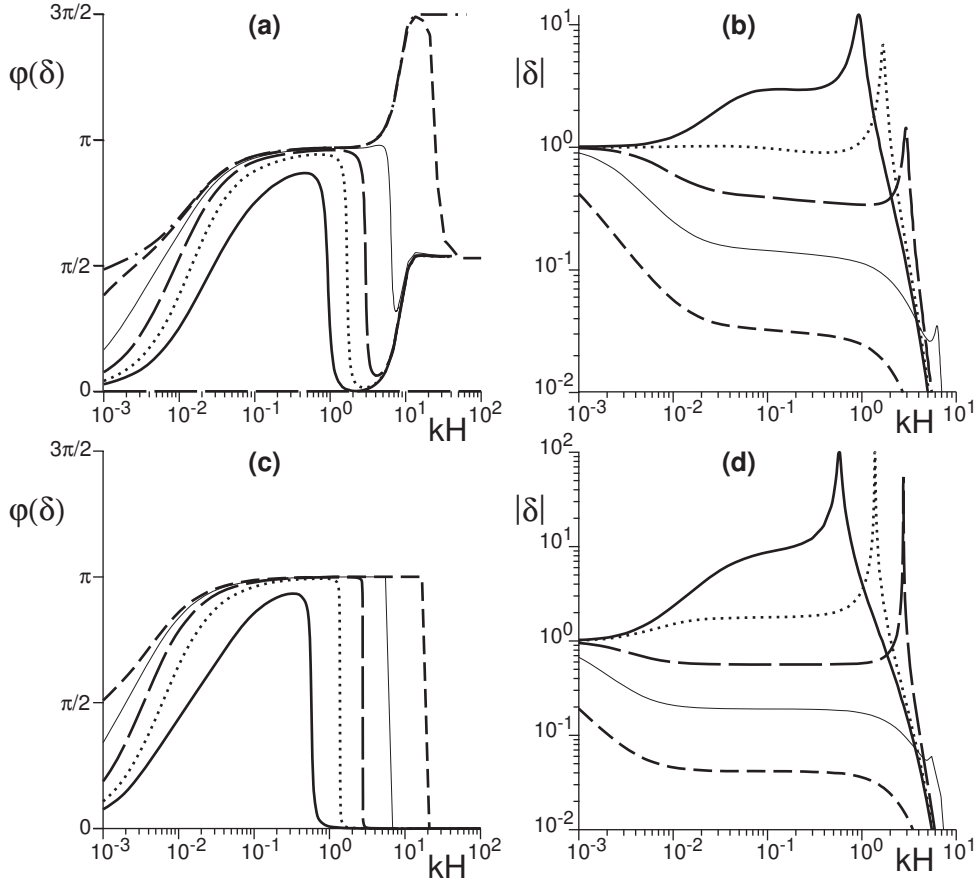


FIGURE 15. The phase (a) and amplitude (b) of the rescaled free surface deformation  $\delta = \Delta/\zeta$  as a function of  $kH$  for  $\mathcal{F} \rightarrow 0$  (dotted dashed line),  $\mathcal{F} = 0.2$  (dashed line),  $\mathcal{F} = 0.4$  (thin solid line),  $\mathcal{F} = 0.6$  (long dashed line),  $\mathcal{F} = 0.8$  (dotted line) and  $\mathcal{F} = 1$  (solid line), and  $H/z_0 = 10^3$ . Crossing the resonance, the phase shifts from 0 to  $\pi$ . (c) and (d), same for the friction force analytical model.

#### 5.4. Results

In order to shed light on the role of the free surface, we have plotted  $A$  and  $B$  as functions of  $\eta_0$  in figure 12. For large enough wave-number  $k$  (small enough wavelength  $\lambda$ ), one recovers the plots of the panels (a) and (b) of figure 6, independently of  $H/z_0$ . This means that for a bottom wavelength much smaller than the flow depth  $H$  (e.g. for subaqueous ripples), the free surface has a marginal effect and the results of section 3 apply. For smaller  $\eta_0$  however, the curves exhibit a peak, whose position depends on the value of  $H/z_0$ , followed by a diverging behaviour when  $\eta_0 \rightarrow 0$ . As discussed below, these peaks can be ascribed to a resonance effect with the free surface, meaning that the proper scale is now  $H$  and not  $z_0$ . As the ratio  $\lambda/H$  is the key parameter separating ripples from dunes, we shall turn extensively in part 3 to this point.

Velocity profiles for different values of  $kH$  are plotted in figure 13. For  $kH$  of order one, as for the unbounded case the flow can be thought of as being divided into two regions: close to the ground where it can be described by the frictional surface layer approximation, and away from the bottom where it behaves like a potential flow. In the latter case, the modes can be decomposed into the sum of decreasing and increasing

exponentials  $e^{\pm\eta}$ . For smaller values of  $kH$ , the potential flow-like region progressively vanishes and the whole flow is controlled by the frictional zone (figure 13(c)).

We display the phase and amplitude of the free surface as a function of  $kH$  in figure 14(b-c). The sharp phase shift as well as the amplitude peak are typical of a resonance effect. For  $kH$  larger than the resonance value, the bottom and the surface are in phase. For smaller  $kH$ , they are in phase opposition. The streamlines in figure 14(a) have precisely been computed for  $\varphi = \pi/2$ . Interestingly, the streamlines are squeezed downstream to the crest at the resonance.

The precise value of  $kH$  at which the resonance occurs depends on the Froude number.  $\varphi$  and  $|\delta|$  are displayed in figure 15 for different values of  $\mathcal{F}$ . One can see that a larger Froude number gives resonating conditions for smaller values of  $kH$ , with a larger peak in amplitude. For very small  $\mathcal{F}$ , the phase curve is more complicated, with an overall shift of  $\pi/2$ . But note that this corresponds to a vanishing amplitude  $\delta$ . For  $kH \rightarrow 0$ , the free surface amplitude seems to converge to some finite value, but the phase slowly goes back to 0. This gentle crossover is indeed expected at very large wavelengths with respect to the water depth, for which the free surface must follow the bottom topography.

The basal shear stress and pressure and subsequently the coefficients  $A$ ,  $B$ ,  $C$  and  $D$  are modified by the presence of the free surface when  $kH$  is of order one and below. In figure 16, the coefficients are plotted *vs*  $kH$  for different values of the Froude number. One can see that these resonance peaks are more pronounced for larger  $\mathcal{F}$  – they are actually not visible when  $\mathcal{F}$  is too small. In agreement with the streamlines of figure 14(a), which shows a squeezing downstream the bump crest, the peak of  $B$  is negative, corresponding to a phase delay of the stress with respect to the bottom. Furthermore, the curves corresponding to the presence of a rigid lid at the same height  $H$  do not exhibit these peaks. Finally, the diverging behaviour of  $B$  as  $kH \rightarrow 0$  is also a free surface effect as, in the same limit,  $B$  reaches a plateau in case of a rigid top boundary.

## 6. A friction force closure

In order to get a better physical understanding of the role of the free surface, we now derive an analytical approximation of the flow field, starting from a very crude turbulent closure. We will show that the properties are interestingly close to those of the above full equations.

### 6.1. Reference state

We start from the Navier-Stokes equations for a perfect flow, with an additional turbulent friction term as an approximation of the stress derivatives:

$$\partial_x u_x + \partial_z u_z = 0, \quad (6.1)$$

$$u_x \partial_x u_x + u_z \partial_z u_x = -\partial_x p + g \sin \theta - \Omega \frac{u_x}{H} u_x, \quad (6.2)$$

$$u_x \partial_x u_z + u_z \partial_z u_z = -\partial_z p - g \cos \theta - \Omega \frac{2u_x}{H} u_z, \quad (6.3)$$

where  $\bar{u}$  is identified below as the mean flow velocity. Physically, the force applied to a fluid particle is directly related to the relative velocity with respect to the ground. At an angle  $\theta$ , the following plug flow is an homogeneous solution of the above equations:

$$u_x = \bar{u} = \sqrt{\frac{gH \sin \theta}{\Omega}}, \quad (6.4)$$

$$u_z = 0, \quad (6.5)$$

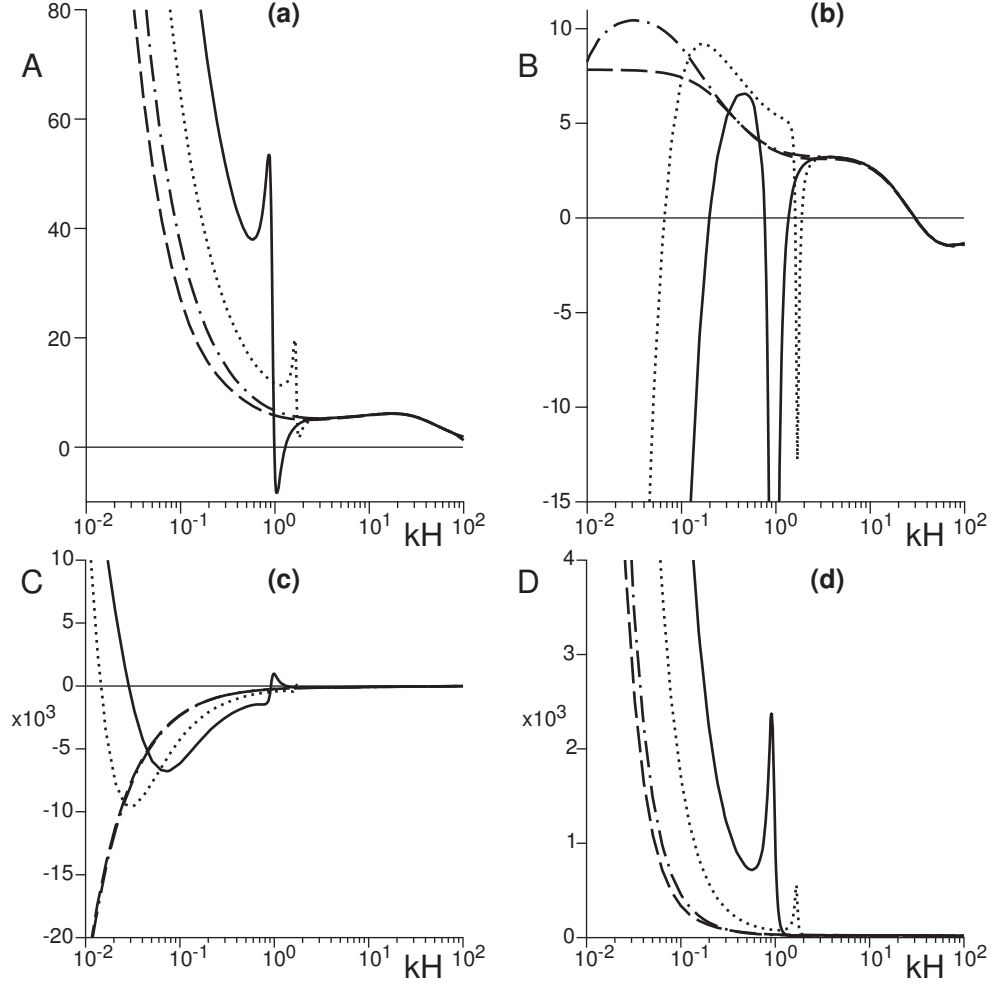


FIGURE 16.  $A$ ,  $B$ ,  $C$  and  $D$  as functions of  $kH$ , for  $\mathcal{F} = 0.1$  (dotted dashed line),  $\mathcal{F} = 0.8$  (dotted line) and  $\mathcal{F} = 1$  (solid line). The dashed lines correspond to a rigid boundary at the same height  $H$ . The plots have been computed for  $H/z_0 = 10^3$ . Comparing a free surface to a rigid boundary condition (or to the case  $H \ll \lambda$ ), it can be inferred that the hydrodynamics is controlled by the surface waves. In particular, the resonance leads to a drop of the shear stress component  $B$  i.e. to a downstream shift of the point of maximum shear stress.)

$$p = g \cos \theta (H - z). \quad (6.6)$$

In order to estimate the value of the friction coefficient, one can make use of the fact that typical turbulent velocity vertical profiles are logarithmic. However, as the logarithm varies slowly when  $z$  is much larger than  $z_0$ , we write  $\bar{u} \sim \frac{1}{H} \int_0^H dz u_x(z) \sim \frac{u_*}{\kappa} \left( \ln \frac{H}{z_0} - 1 \right)$ . Identifying the shear stress on the bottom as  $u_*^2 = gH \sin \theta$ , we finally get with the relation (6.4)

$$\Omega \sim \left( \frac{\kappa}{\ln \frac{H}{z_0} - 1} \right)^2. \quad (6.7)$$

For  $H/z_0$  in the range  $10^3$ - $10^4$ , we get a typical value for  $\Omega$  of the order of few  $10^{-3}$ . We now normalize quantities by  $\bar{u}$  and  $H$  and get a single non-dimensional (Froude) number:

$$\mathcal{F} = \frac{\bar{u}}{\sqrt{gH \cos \theta}}. \quad (6.8)$$

### 6.2. Disturbance

The starting equations can be linearised around the above reference state. Looking at the flow over a corrugated bottom  $Z(x) = \zeta e^{ikx}$ , it is easy to show that the solution is of the following form

$$u_x = \bar{u} + \bar{u}k\zeta e^{ikx} [-a_+ e^{kz} + a_- e^{-kz}], \quad (6.9)$$

$$u_z = \bar{u}ik\zeta e^{ikx} [a_+ e^{kz} + a_- e^{-kz}], \quad (6.10)$$

$$p = g \cos \theta (H - z) + \bar{u}^2 (kH - i2\Omega) \frac{\zeta e^{ikx}}{H} [a_+ e^{kz} - a_- e^{-kz}], \quad (6.11)$$

where  $a_+$  and  $a_-$  must be determined by the boundary conditions. This exponential form is characteristic of potential flows.

### 6.3. Boundary conditions

We require that the velocity normal to the bottom vanishes. Following the notations of the previous sections, we define  $\Delta$  such that the free surface is at the altitude  $H + \Delta$ . It is a material line where the pressure vanishes. The three boundary conditions are then:

$$u_z(z = 0) = i\bar{u}k\zeta e^{ikx}, \quad (6.12)$$

$$u_z(z = H) = i\bar{u}\delta k\zeta e^{ikx}, \quad (6.13)$$

$$p(z = H) = \frac{\bar{u}^2}{H\mathcal{F}^2} \delta \zeta e^{ikx}, \quad (6.14)$$

where we, as before,  $\delta$  is defined as  $\Delta(x) = \delta \zeta e^{ikx}$ . The constants  $a_+$  and  $a_-$ , as well as  $\delta$  are thus solution of

$$a_+ + a_- = 1, \quad (6.15)$$

$$a_+ e^{kH} + a_- e^{-kH} = \delta, \quad (6.16)$$

$$a_+ e^{kH} - a_- e^{-kH} = \frac{\delta}{(kH - i2\Omega)\mathcal{F}^2}, \quad (6.17)$$

from which we get:

$$a_+ = \frac{1}{2} \left[ 1 - \frac{(kH - i2\Omega) \tanh kH - \frac{1}{\mathcal{F}^2}}{(kH - i2\Omega) - \frac{1}{\mathcal{F}^2} \tanh kH} \right], \quad (6.18)$$

$$a_- = \frac{1}{2} \left[ 1 + \frac{(kH - i2\Omega) \tanh kH - \frac{1}{\mathcal{F}^2}}{(kH - i2\Omega) - \frac{1}{\mathcal{F}^2} \tanh kH} \right]. \quad (6.19)$$

### 6.4. Basal shear stress and pressure

The shear stress is not part of the variables of this model, but we can consistently define it as  $\tau = -\Omega u_x^2$ . Looking at the shear stress  $\tau_b$  and normal stress  $p_b$  on the bottom, in accordance with the notations of the previous sections of the paper, we introduce the coefficients  $A$ ,  $B$ ,  $C$  and  $D$  as

$$\tau_b = -\Omega \bar{u}^2 [1 + (A + iB)k\zeta e^{ikx}], \quad (6.20)$$

$$p_b = gH \cos \theta + \Omega \bar{u}^2 (C + iD)k\zeta e^{ikx}, \quad (6.21)$$

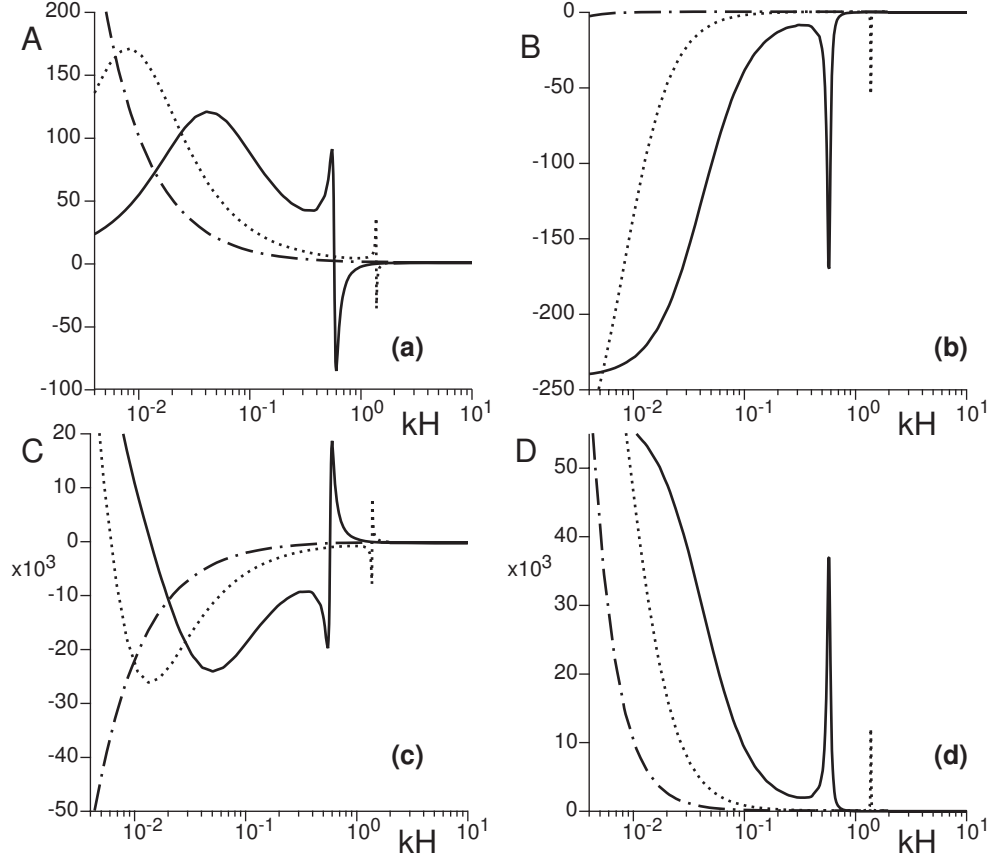


FIGURE 17. Values of the coefficients  $A$ ,  $B$ ,  $C$  and  $D$  predicted by the friction force model as functions of  $kH$ , for  $\mathcal{F} = 0.1$  (dotted dashed line),  $\mathcal{F} = 0.8$  (dotted line) and  $\mathcal{F} = 1$  (solid line). These plots have been computed with  $H/z_0 = 10^3$ .

which gives

$$A = 2 \frac{[(kH)^2 + 4\Omega^2 + \frac{1}{\mathcal{F}^4}] \tanh kH - \frac{1}{\mathcal{F}^2} kH [\tanh^2 kH + 1]}{(kH - \frac{1}{\mathcal{F}^2} \tanh kH)^2 + 4\Omega^2}, \quad (6.22)$$

$$B = \frac{2\Omega}{\mathcal{F}^2} \frac{[\tanh^2 kH - 1]}{(kH - \frac{1}{\mathcal{F}^2} \tanh kH)^2 + 4\Omega^2}, \quad (6.23)$$

$$C = \frac{1}{2\Omega} \left( -A - \frac{2\Omega B}{kH} \right), \quad (6.24)$$

$$D = \frac{1}{2\Omega} \left( -B + \frac{2\Omega A}{kH} \right). \quad (6.25)$$

### 6.5. Results

These coefficients are plotted as a function of  $kH$  in figure 17 for different values of the Froude number. One can notice the presence of the resonance peaks corresponding to the condition:  $\mathcal{F}^2 kH = \tanh kH$ . As the hyperbolic tangent is approximately equal to 1 as soon as  $kH$  is of the order of unity, one immediately gets that the resonant condition

is for

$$(kH)_{\text{res}} \sim \frac{1}{\mathcal{F}^2}. \quad (6.26)$$

This approximation is in good agreement with the solutions of the full equations and gives  $(kH)_{\text{res}}$  between 1 and 20 for Froude numbers in the range 0.2-1. Furthermore, the phase and amplitude of the surface are displayed in figure 15(c)-(d), bearing a remarkable quantitative resemblance with the panels (a) and (b). Boundary conditions corresponding to a rigid lid instead of a free surface at height  $H$  are obtained by setting  $\delta$  to 0 in equation (6.16) and removing equation (6.17) as the pressure would not then be imposed any more. As a result, the solution would be independent of the Froude number with no possibility of generating a peak.

The behaviour of  $A$ ,  $B$ ,  $C$  and  $D$  at small  $kH$  (below the resonance condition) can be also analyzed within this simple model. For  $kH \rightarrow 0$ , but still with  $kH$  (and thus  $1/\mathcal{F}^2$ ) larger than  $\Omega$ , we get  $A \propto 1/(kH)$  and  $B \propto -1/(kH)^2$ . Similarly,  $C \propto 1/(kH)^3$  and  $D \propto 1/(kH)^2$ . These scalings again fit fairly well the solutions of the full equations. For values of  $kH$  even smaller than  $\Omega$ , however, we get that  $A \propto kH$ ,  $B$  and  $D$  tend to constants and  $C$  diverges like  $1/(kH)$ , which are this time specific to the model.

Finally, it is worth noting that the friction force model predicts negative values of  $B$  for any  $kH$ . This means that there is always a phase delay of the shear stress with respect to the bottom, which is a clear disagreement with the full solution (see figure 16(b)). In particular, as will be detailed in the part 3, it cannot describe the ripples primary instability, which is related to an upstream phase shift of the shear stress. In order to fix this flaw, one would need to empirically introduce an imaginary part to  $\Omega$ . Finally, this discrepancy shows that a precise description of the phase between the basal friction and the relief is a subtle and difficult issue that fully justify the use of a rigorous but heavy formalism.

## 7. Conclusion

### 7.1. Summary of the results

The part 1 of this article is focused on the analysis of a turbulent flow over a wavy bottom. The hydrodynamical equations were closed with a second order turbulent closure. Close to the bottom, the full non-linear solution has been derived. When the local shear stress and pressure gradient are antagonist, recirculating flows are obtained. Away from the boundary, we have performed a systematic expansion of the equations with respect to the amplitude of the bottom corrugation  $\zeta$ , up to the third order. We were particularly interested in the basal shear stress profiles, and in the calculation of the phase-lag between the shear and the topography. We found that the bottom corrugation has a negative non-linear feedback on the shear. We also showed that it increases the apparent hydrodynamical roughness. Finally, we study the influence of the presence of a free surface in the situation where the water depth is comparable to the bottom wavelength. We evidenced that, due to the resonance of gravity surface waves, the phase-lag between the shear stress and the bottom profile shifts downstream around  $kH \simeq 1/\mathcal{F}^2$ . A second shift is observed when  $kH \ll 1/\mathcal{F}^2$ . These effects have been recovered within a simple friction force model as a crude stress closure, for which analytical expressions of the linear solution of the flow can be derived.

### 7.2. Towards sediment transport and ripples and dunes formation

The results of this work will serve as inputs in the modeling of sediment transport as well as the understanding of ripples and dunes instabilities. These issues are discussed in the

parts 2 and 3 respectively. In particular, we shall study the relation between the shear stress and the transport, and the corresponding phase-lag between the two. Another important point is the effect of the feedback of transport on the flow. Does it result in a new bottom boundary condition for the flow as suggested by Colombini 2004? Does transport lubricate or increase friction with the bed? With precise hydrodynamical and transport models at hand, one can investigate the mechanisms controlling the formation of sub-aqueous ripples and dunes. Is the dune instability associated to a new destabilizing mechanism induced by the free surface as proposed by Richards 1980 or Colombini 2004, Colombini & Stocchino 2004? What controls the ripple or dune wavelength? We shall see in the part 3 that regions of negative  $B$  correspond to stable bedform wavelength. Finally, our non-linear results will make possible the study of the amplitude selection of the bedforms.

---

The fundamental reason for the upstream shift of the maximum shear stress was meditated with Brad Murray. This work has benefited from the support of the french minister of research with an ‘ACI Jeunes Chercheurs’. We thank l’Éouvé for hospitality, where part of this paper was written.

## Appendix A. Representation of the disturbances

### A.1. Linear order

Recall that  $Z(x) = \zeta e^{ikx}$  is the bottom profile whose wavelength is  $\lambda = 2\pi/k$ , and  $\eta = kz$  the dimensionless vertical coordinate. At the linear order, we write all the relevant quantities under the form:

$$f = \bar{f}(\eta) + k\zeta e^{ikx} f_1(\eta). \quad (\text{A } 1)$$

An alternative is to use the curvilinear coordinates  $\xi = \eta - kZ$  and write the field  $f$  as:

$$f = \bar{f}(\xi) + k\zeta e^{ikx} \tilde{f}_1(\xi). \quad (\text{A } 2)$$

We call these expressions respectively the ‘non-shifted’ and ‘shifted’ representations of  $f$ . They lead to the same linearised equations as they are related to each other at the linear order by

$$\tilde{f}_1 = f_1 + \bar{f}'. \quad (\text{A } 3)$$

In practice, this is especially relevant for  $U$ , for which  $\bar{f} = \mu$  is not constant:  $\tilde{U} = U + \mu'$  is the shifted representation of the first order correction to the horizontal velocity. However,  $\tilde{W} = W$ ,  $\tilde{S}_t = S_t$  and  $\tilde{S}_n = S_n$ . Importantly, note that the range in  $\eta$  for which these two representations are valid is not the same *a priori*.

### A.2. Representations for the non-linear expansion

All fields are expanded up to the third order in  $k\zeta$ , neglecting also non-harmonic terms in  $(k\zeta)^3 e^{\pm i3kx}$ . Non-shifted representation of the streamwise velocity:

$$\frac{u_x}{u_*} = \mu(\eta) + (k\zeta)e^{ikx}U_1(\eta) + (k\zeta)^2U_0(\eta) + (k\zeta)^2e^{2ikx}U_2(\eta) + (k\zeta)^3e^{ikx}U_3(\eta). \quad (\text{A } 4)$$

Shifted representation of the same quantity:

$$\frac{u_x}{u_*} = \mu(\xi) + (k\zeta)e^{ikx}\tilde{U}_1(\xi) + (k\zeta)^2\tilde{U}_0(\xi) + (k\zeta)^2e^{2ikx}\tilde{U}_2(\xi) + (k\zeta)^3e^{ikx}\tilde{U}_3(\xi). \quad (\text{A } 5)$$

Expanding the functions  $\tilde{f}_\alpha(\eta - k\zeta e^{ikx})$  with respect to  $k\zeta$ , one can relate a representation to the other as:

$$U_1 = \tilde{U}_1 - \mu', \quad (\text{A } 6)$$

$$U_0 = \tilde{U}_0 + \frac{1}{4}\mu'' - \frac{1}{4}(\tilde{U}'_1 + \tilde{U}'_1{}^*), \quad (\text{A } 7)$$

$$U_2 = \tilde{U}_2 + \frac{1}{4}\mu'' - \frac{1}{2}\tilde{U}'_1, \quad (\text{A } 8)$$

$$U_3 = \tilde{U}_3 - \frac{1}{8}\mu''' - \tilde{U}'_0 - \frac{1}{2}\tilde{U}'_2 + \frac{1}{4}\tilde{U}''_1 + \frac{1}{8}\tilde{U}''_1{}^*. \quad (\text{A } 9)$$

Conversely:

$$\tilde{U}_1 = U_1 + \mu', \quad (\text{A } 10)$$

$$\tilde{U}_0 = U_0 + \frac{1}{4}\mu'' + \frac{1}{4}(U'_1 + U'_1{}^*), \quad (\text{A } 11)$$

$$\tilde{U}_2 = U_2 + \frac{1}{4}\mu'' + \frac{1}{2}U'_1, \quad (\text{A } 12)$$

$$\tilde{U}_3 = U_3 + \frac{1}{8}\mu''' + \frac{1}{4}U''_1 + \frac{1}{8}U''_1{}^* + U'_0 + \frac{1}{2}U'_2. \quad (\text{A } 13)$$

The passage from a representation to the other for the other fields works the same, except that there is no zeroth order (function  $\mu$ ) in the expressions.

## Appendix B. Stream function

To compute the streamlines, we introduce the so-called stream function  $\Psi(x, z)$ , defined by  $\partial\Psi/\partial x = -u_z$  and  $\partial\Psi/\partial z = u_x$ . This function is such that  $\vec{u} \cdot \vec{\nabla}\Psi = 0$ , so that the isocontours  $\Psi = \text{Cst}$  precisely show the streamlines. Using the continuity equation (2.10), it is easy to show that a solution is  $\Psi = \int d\tilde{z} u_x$ . This integral is computed between  $\tilde{z} = Z$  (the bottom) and  $\tilde{z} = z$ . Noting that  $U = iW'$  (equation (3.20)), we end up with

$$\Psi = \frac{u_*}{k} \{ (\eta - kZ) [\mu(\eta - kZ) - 1] + k\zeta e^{ikx} [iW(\eta - kZ) + \mu(\eta - kZ)] \}. \quad (\text{B } 1)$$

In the situation with a free surface, one can use the following representation for the field  $f$ :

$$f = \bar{f}(\xi) + k\zeta e^{ikx} \tilde{f}_1(\xi), \quad \text{with} \quad \xi = \eta_H \frac{z - Z}{H + \Delta - Z}. \quad (\text{B } 2)$$

This curvilinear variable  $\xi$  vanishes on the bottom  $z = Z$ , and  $\xi = \eta_H$  at the surface  $z = H + \Delta$ . The new function  $\tilde{f}_1$  is related to those of the non-shifted representation  $\bar{f}$  and  $f_1$  as:

$$\tilde{f}(\xi) = f_1(\xi) + \left( 1 + (\delta - 1) \frac{\xi}{\eta_H} \right) \bar{f}'(\xi). \quad (\text{B } 3)$$

For  $f = u_x$ , we have  $\bar{f} = \mu$  and  $f_1 = U = iW'$ . Consequently, the new stream function is

$$\Psi_{FS} = \frac{u_*}{k} \left\{ \xi [\mu(\xi) - 1] + k\zeta e^{ikx} \left[ iW(\xi) + \mu(\xi) + (\delta - 1) \frac{\xi \mu(\xi)}{\eta_H} \right] \right\}. \quad (\text{B } 4)$$

One can check that the free surface is indeed a streamline itself, as one of the top boundary conditions is  $W(\eta_H) = i\mu(\eta_H)\delta$ .

### Appendix C. Weakly non-linear calculations

Definition of the different functions involved in the expansion:

$$u_x = u_* \left[ \mu + (k\zeta)e^{ikx}U_1 + (k\zeta)^2U_0 + (k\zeta)^2e^{2ikx}U_2 + (k\zeta)^3e^{ikx}U_3 \right], \quad (C1)$$

$$u_z = u_* \left[ (k\zeta)e^{ikx}W_1 + (k\zeta)^2e^{2ikx}W_2 + (k\zeta)^3e^{ikx}W_3 \right], \quad (C2)$$

$$\tau_{xz} = -u_*^2 \left[ 1 + (k\zeta)e^{ikx}S_{t1} + (k\zeta)^2S_{t0} + (k\zeta)^2e^{2ikx}S_{t2} + (k\zeta)^3e^{ikx}S_{t3} \right], \quad (C3)$$

$$p + \tau_{zz} = p_0 + u_*^2 \left[ (k\zeta)e^{ikx}S_{n1} + (k\zeta)^2S_{n0} + (k\zeta)^2e^{2ikx}S_{n2} + (k\zeta)^3e^{ikx}S_{n3} \right], \quad (C4)$$

$$\tau_{zz} - \tau_{xx} = u_*^2 \left[ (k\zeta)e^{ikx}S_{d1} + (k\zeta)^2S_{d0} + (k\zeta)^2e^{2ikx}S_{d2} + (k\zeta)^3e^{ikx}S_{d3} \right]. \quad (C5)$$

Expansion of the mixing length:

$$\kappa^2(kL)^2 = \frac{1}{\mu'^2} - \frac{2\kappa}{\mu'}(k\zeta)e^{ikx} + \frac{\kappa^2}{2}(k\zeta)^2 + \frac{\kappa^2}{2}(k\zeta)^2e^{2ikx}. \quad (C6)$$

Expansion of the strain tensor components:

$$\dot{\gamma}_{xx} = 2 \left[ (k\zeta)e^{ikx}iU_1 + (k\zeta)^2e^{2ikx}2iU_2 + (k\zeta)^3e^{ikx}iU_3 \right], \quad (C7)$$

$$\dot{\gamma}_{zz} = -\dot{\gamma}_{xx}, \quad (C8)$$

$$\begin{aligned} \dot{\gamma}_{xz} = & \mu' + (k\zeta)e^{ikx}(U'_1 + iW_1) + (k\zeta)^2U'_0 + (k\zeta)^2e^{2ikx}(U'_2 + 2iW_2) \\ & + (k\zeta)^3e^{ikx}(U'_3 + iW_3), \end{aligned} \quad (C9)$$

which gives for the strain modulus:

$$\begin{aligned} |\dot{\gamma}| = & \mu' + (k\zeta)e^{ikx}(U'_1 + iW_1) + (k\zeta)^2 \left[ U'_0 + \frac{U_1U_1^*}{\mu'} \right] + (k\zeta)^2e^{2ikx} \left[ U'_2 + 2iW_2 - \frac{U_1^2}{\mu'} \right] \\ & + (k\zeta)^3e^{ikx} \left[ U'_3 + iW_3 - \frac{U_1U_1^*}{\mu'^2}(U'_1 + iW_1) + \frac{U_1^2}{2\mu'^2}(U_1^* - iW_1^*) + \frac{4U_1^*U_2}{\mu'} \right], \end{aligned} \quad (C10)$$

and then

$$\begin{aligned} \kappa^2(kL)^2|\dot{\gamma}| = & \frac{1}{\mu'} + (k\zeta)e^{ikx} \left[ \frac{1}{\mu'^2}(U'_1 + iW_1) - 2\kappa \right] \\ & + (k\zeta)^2 \left[ \frac{\kappa^2\mu'}{2} - \frac{\kappa}{2\mu'}(U'_1 + U_1^* + iW_1 - iW_1^*) + \frac{1}{\mu'^2} \left( U'_0 + \frac{U_1U_1^*}{\mu'} \right) \right] \\ & + (k\zeta)^2e^{2ikx} \left[ \frac{\kappa^2\mu'}{2} - \frac{\kappa}{\mu'}(U'_1 + iW_1) + \frac{1}{\mu'^2} \left( U'_2 + 2iW_2 - \frac{U_1^2}{\mu'} \right) \right] \\ & + (k\zeta)^3e^{ikx} \left[ \frac{\kappa^2}{4}(2U'_1 + U_1^* + 2iW_1 - iW_1^*) - \frac{\kappa}{\mu'} \left( 2U'_0 + \frac{U_1(2U_1^* - U_1)}{\mu'} + U'_2 + 2iW_2 \right) \right] \\ & + \frac{1}{\mu'^2} \left( U'_3 + iW_3 - \frac{U_1U_1^*}{\mu'^2}(U'_1 + iW_1) + \frac{U_1^2}{2\mu'^2}(U_1^* - iW_1^*) + \frac{4U_1^*U_2}{\mu'} \right). \end{aligned} \quad (C11)$$

Expressions of the different functions corresponding to the normal stresses  $\tau_{zz} - \tau_{xx}$ :

$$S_{d1} = \frac{4i}{\mu'}U_1, \quad (C12)$$

$$S_{d0} = \frac{i}{\mu'^2} (U_1(U_1^* - iW_1^*) - U_1^*(U'_1 + iW_1)) + 2i\kappa(U_1^* - U_1), \quad (C13)$$

$$S_{d2} = \frac{8i}{\mu'}U_2 + \frac{2i}{\mu'^2}U_1(U'_1 + iW_1) - 4i\kappa U_1, \quad (C14)$$

$$S_{d3} = \frac{4i}{\mu'}U_3 + \frac{4i}{\mu'^2}U_2(U_1^* - iW_1^*) - 8i\kappa U_2 + i\kappa^2\mu'(2U_1 - U_1^*) + \frac{6i}{\mu'^3}U_1^2U_1^* \quad (C15)$$

$$+ \frac{2i\kappa}{\mu'}(U_1' + iW_1)(U_1^* - U_1) - \frac{2i\kappa}{\mu'}U_1(U_1'^* - iW_1^*) + \frac{4i}{\mu'^2}U_1U_0' - \frac{2i}{\mu'^2}U_1^*(U_2' + 2iW_2).$$

Expressions of the different  $\vec{S}_\alpha$ :

$$\vec{S}_1 = \begin{pmatrix} \kappa\mu'^2 \\ 0 \\ 0 \\ 0 \end{pmatrix}, \quad (\text{C } 16)$$

$$\vec{S}_0 = \begin{pmatrix} -\frac{\kappa^2\mu'^3}{4} - \frac{1}{4\mu'}(U_1' + iW_1)(U_1'^* - iW_1^*) \\ \quad + \frac{\kappa\mu'}{2}(U_1' + U_1'^* + iW_1 - iW_1^*) - \frac{1}{2\mu'}U_1U_1^* \\ 0 \\ \frac{1}{4}(W_1U_1'^* + W_1^*U_1') \\ \frac{i}{2}(U_1W_1^* - U_1^*W_1) \end{pmatrix}, \quad (\text{C } 17)$$

$$\vec{S}_2 = \begin{pmatrix} -\frac{\kappa^2\mu'^3}{4} - \frac{1}{4\mu'}(U_1' + iW_1)^2 + \kappa\mu'(U_1' + iW_1) + \frac{1}{2\mu'}U_1^2 \\ 0 \\ \frac{1}{2}W_1U_1' + \frac{i}{2}U_1^2 + \frac{4}{\mu'^2}U_1(U_1' + iW_1) - 8\kappa U_1 \\ 0 \end{pmatrix}, \quad (\text{C } 18)$$

$$\vec{S}_3 = \begin{pmatrix} 2\kappa\mu'U_0 + \frac{\kappa}{2}U_1(2U_1^* - U_1) + \kappa\mu'(U_2' + 2iW_2) - \frac{2}{\mu'}U_1^*U_2 \\ \quad - \frac{\mu'}{2}(U_1' + iW_1) \left[ \kappa^2\mu' - \frac{\kappa}{2\mu'}(U_1' + 2U_1'^* + iW_1 - 2iW_1^*) + \frac{2}{\mu'^2}U_0' \right] \\ \quad - \frac{\mu'}{4}(U_1'^* - iW_1^*) \left[ \kappa^2\mu' + \frac{2}{\mu'^2}(U_2' + 2iW_2) \right] \\ 0 \\ iU_0U_1 + \frac{i}{2}U_2U_1^* + U_0'W_1 + \frac{1}{2}W_1^*U_2' + \frac{1}{2}W_2U_1'^* \\ \quad + \frac{4}{\mu'^2}U_2(U_1'^* - iW_1^*) - 8\kappa U_2 + \kappa^2\mu'(2U_1 - U_1^*) + \frac{6}{\mu'^3}U_1^2U_1^* \\ \quad + \frac{2\kappa}{\mu'}(U_1' + iW_1)(U_1^* - U_1) - \frac{2\kappa}{\mu'}U_1(U_1'^* - iW_1^*) + \frac{4}{\mu'^2}U_1U_0' \\ \quad - \frac{2}{\mu'^2}U_1^*(U_2' + 2iW_2) \\ -iU_0'W_1 - \frac{3i}{2}W_2U_1^* + \frac{3i}{2}U_2W_1^* \end{pmatrix} \quad (\text{C } 19)$$

## REFERENCES

- Andreotti, B., Claudin, P. & Douady, S., Selection of dune shapes and velocities. Part 2: A two-dimensional modelling, *Eur. Phys. J. B* (2002), vol. 28, pp 341-352.
- Ayotte, K.W., Xu, D. & Taylor, P.A., The impact of turbulence closure schemes on predictions of the mixed spectral finite-difference model for flow over topography, *Boundary-Layer Meteo.* (1994), vol 68, pp 1-33.
- Charru, F. & Hinch, E. J., 'Phase diagram' of interfacial instabilities in a two-layer Couette flow and mechanism for the long-wave instability, *J. Fluid. Mech.* (2000), vol. 414, pp. 195-223.
- Coleman, S.E. & Fenton, J.D., Potential-flow instability theory and alluvial stream bed forms, *J. Fluid. Mech.*(2000), vol. 418, pp. 101-117.
- Colombini, M., Revisiting the linear theory of sand dune formation, *J. Fluid. Mech.* (2004), vol. 502, pp. 1-16.
- Colombini, M. & Stocchino, A., Coupling or decoupling bed and flow dynamics: Fast and slow sediment waves at high Froude numbers, *Phys. Fluids* (2005), vol. 17, 036602.
- Engelund, F., Instability of erodible beds, *J. Fluid. Mech.* (1970), vol. 42, pp. 225-244.
- Engelund, F. & Fredsøe, J., Three-dimensionnal stability analysis of open channel flow over an erodible bed., *Nordic Hydrology* (1971), vol. 2, pp. 93-108.
- Fredsøe, J., On the development of dunes in erodible channels, *J. Fluid. Mech.* (1974), vol. 64, pp. 1-16.
- Gong, W., Taylor, P.A. & Dörnbrack, A., Turbulent boundary-layer flow over fixed aerody-

- namically rough two-dimensional sinusoidal waves, *J. Fluid. Mech.* (1996), vol. 312, pp. 1-37.
- Gradowczyk, M.H., Wave propagation and boundary instability in erodible-bed channels, *J. Fluid Mech.* (1970), vol. 33, pp. 93-112.
- Henn, D.S. & Sykes, R.L., Large-eddy simulation of slow over wavy surfaces, *J. Fluid. Mech.* (1999), vol. 383, pp. 75-112.
- Jackson, P.S. & Hunt, J.C.R., Turbulent wind flow over a low hill, *Q. J. R. Meteorol. Soc.* (1975), vol. 101, 929.
- Kennedy, J.F., The mechanics of dunes and antidunes in erodible bed channels., *J. Fluid. Mech.* (1963), vol. 16, pp. 521-544.
- Kroy, K., Sauermann, G. & Herrmann, H.J., Minimal model for aeolian sand dunes, *Phys. Rev. E* (2002), vol. 66, 031302.
- Parker, G., Sediment inertia as cause of river antidunes, *J. Hydraul. Div. ASCE* (1975), vol. 101, pp. 211-221.
- Poggi, D. , Katul, G.G., Albertson, J.D. & Ridolfi, L., An experimental investigation of turbulent flows over a hilly surface, *Phys. Fluids* (2007), vol. 19, 036601.
- Prandtl, L., Bericht ueber Untersuchungen zur ausgebildeten Turbulenz, *ZAMM* (1925), vol 3, pp 136-139.
- Reynolds, A.J., Waves on the erodible bed of an open channel, *J. Fluid Mech.* (1965), vol. 22, pp. 113-133.
- Reynolds, O., On the extent and action of the heating surface of steam boilers, *Proc. Manchester Lit. Phil. Soc.* (1874), vol 8.
- Richards, K.J., The formation of ripples and dunes on an erodible bed, *J. Fluid. Mech.* (1980), vol. 99, pp. 597-618.
- Smith, J.D., Stability of a sand bed subjected to a shear flow at low Froude number, *J. Geophys. Rev.* (1970), vol. 75, pp. 5928-5940.
- Tritton, D.J., *Physical fluid dynamics*, Oxford University Press (1988).
- Wiggs, G.F.S., Desert dune processes and dynamics, *Progress in physical geography* (2002), vol. 25, pp 53-79.